Fermi National Accelerator Laboratory

MAD/PH/547
FERMILAB-PUB-89/243-T
December 1989

Higgs Boson Production at Large Transverse Momentum in Hadronic Collisions

U. Baur

Physics Department, University of Wisconsin
Madison, WI 53706, USA

and

E. W. N. Glover

Fermi National Accelerator Laboratory
P. O. Box 500, Batavia, IL 60510, USA

ABSTRACT

Production of Higgs bosons accompanied by a large transverse momentum jet at hadron colliders via a top quark loop is calculated to lowest order QCD. Analytic expressions for the matrix elements, including the decay $H \to VV \to 4$ massless fermions ($V = W, Z$), are presented. The dependence of the matrix elements on the mass of the top quark exchanged in the loop in all regions of phase space is studied in detail. The Hj signal is compared with the background arising from VVj and V+3 jet production for LHC and SSC energies.

1 Introduction

One of the predictions of the standard model of electroweak interactions is the presence of a Higgs boson of unspecified mass. The discovery of such a Higgs boson would provide a crucial test of the standard model and the search for the Higgs boson is therefore one of the major experimental goals of the next decade or so. There are different search strategies depending on the Higgs boson mass, m_H. Light Higgs bosons may be found at LEPI through the decay $Z \to H\mu^+\mu^-$ [1] ($m_H \lesssim 50$ GeV) or at LEPII via the process $e^+e^- \to ZH$ [2] ($m_H \lesssim 80$ GeV). For more massive Higgs bosons, there are two distinct mass regions. For m_H less than twice the W boson mass M_W the Higgs boson will mainly decay into $q\bar{q}$ states. At hadron colliders the Higgs signal in the region $m_H < 2M_W$ is overwhelmed by QCD background and an e^+e^- collider with $\sqrt{s} = 300 - 400$ GeV offers a much better chance to discover the Higgs boson in this mass range. Only rare decay modes such as the decays $H \to \gamma\gamma$ or $H \to Z\gamma$ [3] which proceed via quark loops offer some hope to discover the Higgs boson in the region $m_H < 2M_W$ at a hadron collider. These machines do much better in searching for the Higgs in the second, heavy Higgs, mass region ($m_H > 2M_W$). The dominant decay modes are then $H \to ZZ$, $H \to W^+W^-$ and $H \to t\bar{t}$ and the event rates are sufficiently high for the 'gold-plated' $H \to ZZ \to \ell^+\ell^-\ell'^+\ell'^-$ decay mode ($\ell = e,\ \mu$) to be visible for $m_H \leq 300\,(600)$ GeV at the LHC (SSC) (pp colliders with $\sqrt{s} = 16$ TeV and $\sqrt{s} = 40$ TeV respectively) assuming an integrated luminosity of 10^4 pb^{-1} [4]. Higher integrated luminosities, or less clean decay modes, may allow the region 600 GeV $< m_H <$ 1000 GeV to be explored at either the SSC or LHC [5].

The dominant Higgs boson production mechanisms in hadron colliders are gluon fusion [6],

$$gg \to H, \tag{1.1}$$

where the gluons couple to a top quark loop, and WW fusion [7],

$$qq \to qqH, \tag{1.2}$$

where the initial quarks each radiate a W boson which annihilate to produce the Higgs boson. The cross section for the gluon fusion process depends strongly on the unknown top quark mass m_t, however, for $m_t > 80$ GeV [8], the gluon fusion process dominates for $m_H \lesssim 600$ GeV at the SSC. At larger Higgs boson masses, the WW fusion process becomes important. The two processes are topologically different, since, to lowest order, the Higgs bosons produced from gluon fusion have small transverse momentum, p_T, while those from WW fusion have $p_T \sim M_W$ balanced by the two small angle quark jets. This transverse motion (along with the possibility of tagging the quark jets [9]) has been proposed [10] as a discriminant against the background for the favoured decay mode, $H \rightarrow ZZ$, where the dominant backgrounds,

$$q\bar{q} \rightarrow ZZ, \tag{1.3}$$

and [11],

$$gg \rightarrow ZZ, \tag{1.4}$$

also lead to a ZZ pair with small transverse momentum.

In general, however, once higher order corrections are taken into account, the Higgs bosons produced by the gluon fusion process (1.1) will have a non-negligible transverse momentum. The large p_T region is well described by the $O(\alpha_s^3)$ processes,

$$gg \rightarrow gH, \quad qg \rightarrow qH, \tag{1.5}$$

and,

$$q\bar{q} \rightarrow gH, \tag{1.6}$$

shown in Fig. 1. As in the $O(\alpha_s^2)$ process (1.1), there is a large dependence on the top quark mass.

In this paper we will study the production of a Higgs boson accompanied by a large p_T jet via the processes (1.5) and (1.6). The matrix elements for these processes were first calculated in ref. [12] which was mainly concerned with the possibility of using the $H \rightarrow \tau^+\tau^-$ decay of a large p_T Higgs boson as a signal in the intermediate Higgs mass region. In our work we extend the analysis of ref. [12] to heavy Higgs bosons with $m_H > 2M_W$. Our analysis divides into two parts. In the first, we make a detailed study of how the mass of the top quark affects the matrix elements in all regions of phase space and show how this translates to the observable p_T distribution. In particular, we develop two approximations to the matrix elements, when the top quark mass is either large compared to all other kinematic quantities, or when it is small. For heavy Higgs bosons, $m_H > 2M_W$, as we will show, the large mass approximation grossly overestimates the cross-section at large p_T for all values of m_t, 80 GeV $< m_t <$ 200 GeV. On the other hand, the small mass approximation gives a reasonable estimate of the exact result over most of phase space for a wide range of m_t.

The second part is devoted to a phenomenological comparison of the Higgs boson signal accompanied by a large p_T jet with the background at the SSC and LHC. Analytic expressions for the matrix elements, including the decay $H \to VV \to f_1\bar{f}_2f_3\bar{f}_4$ where $V = W$, Z and $f_1 \ldots f_4$ are massless fermions are presented. At large p_T, the rate for Higgs boson production is $O(\alpha_s)$ compared to the production rate at small p_T, so that the potential for observing a heavy Higgs through the 'gold-plated' $H \to ZZ \to \ell^+\ell^-\ell'^+\ell'^-$ mode is significantly reduced. On the other hand, one could recoup this factor if one of the Z bosons is allowed to decay hadronically. In this case there is an additional background from the production of a Z boson in association with 3 hadronic jets. Some of the time, two of the jets will have an invariant mass close to M_Z thus generating a 'fake' background which depends on the detector resolution. For a representative choice of lepton and jet identification criteria we make a comparison of the $H \to ZZ \to \ell^+\ell^-q\bar{q}$ signal and the 'real' and 'fake' backgrounds. A similar analysis is also presented for $H \to W^+W^- \to \ell^\pm\nu q\bar{q}$. Finally, in section 4, we shall summarize our results.

2 Top Quark Mass Dependence

In order to compute the production cross section for a Higgs boson with large transverse momentum, the matrix elements for (1.5) and (1.6) have to be calculated. This was first carried out in ref. [12]. We have repeated the calculation, using the methods of ref. [13] to express the contributing helicity amplitudes as combinations of scalar one loop integrals. The scalar integrals may then be expressed in terms of complex Spence functions [14]. We find complete agreement with ref. [12], however, since we use a rather different notation we present the helicity amplitudes in Appendix A, while the expressions for the scalar integrals are given in Appendix B.

The form of the cross section is rather complicated, and, in order to gain some insight on the top quark mass dependence, we show the squared matrix elements for each of the three processes in Fig. 2 as a function of m_t/m_H. For simplicity, we consider only right-angle scattering at fixed centre of mass energy, $\hat{s} = 4m_H^2$ and $\hat{u} = \hat{t}$. $\hat{s}$, $\hat{t}$ and $\hat{u}$ are the usual Mandelstam variables. Furthermore, we keep only the contribution from the top quark. The three curves are normalised so that as $m_t \to \infty$, $|\mathcal{M}|^2 \to 1$. In this heavy top quark limit, the loop integrals simplify considerably,

$$\begin{aligned}
D(x,y) &\rightarrow \frac{1}{6m_t^4} + O\left(\frac{1}{m_t^6}\right), \\
C(x) &\rightarrow -\frac{1}{2m_t^2} - \frac{x}{24m_t^4} + O\left(\frac{1}{m_t^6}\right), \\
B_1(x) &\rightarrow \frac{x - m_H^2}{6m_t^2} + O\left(\frac{1}{m_t^4}\right).
\end{aligned} \tag{2.1}$$

Since the top quark coupling to the Higgs boson is proportional to the mass, the ggH and $gggH$ couplings do not vanish but tend to a constant and may be generated by the effective Lagrangian,

$$\mathcal{L}_{eff} = \frac{\alpha_s}{12\pi} \frac{g_W}{2M_W} G^{a\mu\nu} G^a_{\mu\nu} H , \tag{2.2}$$

where $G^a_{\mu\nu}$ is the gluon field strength tensor and H is the Higgs field. The matrix elements are then extremely simple [12] (see Eqs. (A.24) and (A.25)).

On the other hand, as $m_t \rightarrow 0$, the triangle and box integrals depend logarithmically on the quark mass,

$$D(x,y) \sim \frac{1}{xy} \log^2(m_t^2) , \quad C(x) \sim \frac{1}{2x} \log^2(m_t^2) , \tag{2.3}$$

and the cross section for all three processes vanishes as,

$$|\mathcal{M}|^2 \sim m_t^4 \log^4(m_t^2) . \tag{2.4}$$

These two limits are separated by the region where $m_t \sim m_H$ which contains two thresholds. Above a threshold, the particles circulating in the loop are always virtual while below the threshold they may be on-shell. A threshold is therefore always associated with the turning on or off of an imaginary piece and a corresponding shape change in the matrix elements. The first threshold corresponds to the situation when the the top quarks coupling to the Higgs boson may be real and occurs at $2m_t = m_H$. The second, is associated with the possibility of making a cut in the $\hat{s}$-channel to produce real top quarks and happens when $2m_t = \sqrt{\hat{s}}$. Due to the particular choice of $\hat{s}$ in Fig. 2, these thresholds appear at $m_t/m_H = 0.5$ and 1 respectively.

Figure 2a shows both of these thresholds for the process $gg \rightarrow gH$ while the two other processes only show one. The reasons for this are quite straightforward. In the case of the $\hat{t}$-channel exchange $qg \rightarrow qH$ process, it is not possible to make the $\hat{s}$-channel cut (see Fig. 1b), while in the $q\bar{q} \rightarrow gH$ case, the imaginary pieces are proportional to the combination,

$$\theta(\hat{s} - 4m_t^2) - \theta(m_H^2 - 4m_t^2). \tag{2.5}$$

At the first threshold, $m_t/m_H = 0.5$, the imaginary piece switches on and causes the rapid growth in the region $0.5 < m_t/m_H < 1.0$, while at the second, the imaginary piece suddenly switches off causing an abrupt drop.

Clearly, in the threshold region the matrix elements are rapidly changing, however, they are well behaved in both the small and large quark mass regions. This fact has encouraged us to develop two approximations, one for use in each region. In the large mass aproximation, the matrix elements themselves reduce to rather compact forms [12], while in the small mass limit the scalar integrals simplify. They are listed in Appendix C. In particular both the top quark mass dependence and the imaginary pieces are isolated. The few remaining Spence functions have simple arguments well away from the branch cut and are easy to evaluate.

In Figs. 3 and 4 we investigate the accuracy of these approximations over the whole of phase space, and, since the cross section is dominated by the $gg \rightarrow gH$ process, we show only the gg contribution. Figure 3 shows the exact matrix elements for $\hat{u} = \hat{t} = (m_H^2 - \hat{s})/2$ normalised to the large mass limit (Fig. 3a) and the small mass limit (Fig. 3b) as a function of p_T/m_t for various values of m_H/m_t where p_T is the transverse momentum of the Higgs boson:

$$p_T^2 = \frac{\hat{u}\hat{t}}{\hat{s}} \,. \tag{2.6}$$

As can be clearly seen in Fig. 3a, the large mass limit only works well when both p_T/m_t and m_H/m_t are small. At large values of p_T, however, the large mass approximation breaks down since there are now two large scales (p_T and m_t) in the problem and drastically overestimates the cross section. This is rather unfortunate since the $O(\alpha_s^3)$ processes (1.5) and (1.6) only provide a good description of the Higgs boson p_T distribution at large p_T. At small transverse momenta the cross section diverges, and virtual and multiple gluon emission processes become important. On the other hand, for large values of m_H/m_t the small mass expansion is a good approximation over nearly all of the p_T range, only breaking down at $p_T \ll m_t$. Furthermore, even for $m_H \ll m_t$ the approximation becomes better with increasing p_T. Figure 3 also serves to illustrate the fact that at large p_T, the transverse momentum distribution is essentially independent of m_H.

Figure 4 shows that in the regions where the approximations work at all, they are valid over all possible values of the centre-of-mass jet rapidity,

$$y_j^* = \frac{1}{2}\log\left(\frac{\hat{t}}{\hat{u}}\right) . \tag{2.7}$$

For the currently prefered range of top quark masses, 80 GeV $< m_t <$ 200 GeV [8, 15], and heavy Higgs bosons, $m_H > 2M_W$, one expects the small mass expansion to work rather better than the large mass expansion particularly at large p_T and large m_H.

In practice, however, the observable cross section is obtained by integrating over all values of $\hat{s}$ weighted by the structure functions. As we will show, the general behaviour observed for the matrix elements does not change. Furthermore, since the width of heavy Higgs bosons is quite large, finite width effects might be appreciable and it is also necessary to study the effect of the Higgs decay. The dominant decay modes of a heavy Higgs boson are $H \to ZZ$, $H \to WW$ and $H \to t\bar{t}$, and, due to overwhelming QCD backgrounds, the cleanest signature is the decay into four charged leptons,

$$H \to ZZ \to \ell^+\ell^-\ell'^+\ell'^-. \tag{2.8}$$

Since the Higgs boson is a scalar, it is straightforward to modify the on-shell matrix elements to incorporate the subsequent decay and this is described in Appendix A.

In Fig. 5 we show the transverse momentum distribution for the process,

$$pp \to H + jet \to ZZ + jet, \tag{2.9}$$

for pp collisions at $\sqrt{s} = 40$ TeV. For the numerical results presented here and throughout the rest of the paper, we use set 1 of the Duke-Owens structure functions [16] and the running strong coupling constant with $\Lambda = 0.2$ GeV evaluated at $Q^2 = \hat{s}/4$. The choice of scale is somewhat arbitrary and, since we are dealing with an $O(\alpha_s^3)$ process, different choices may alter the results by as much as a factor of two. Furthermore, we neglect the extremely small contribution from the light quarks in addition to any potentially large effect from extra heavy generations. For the electroweak parameters we use $M_Z = 91.1$ GeV, $M_W = 80.0$ GeV, $\sin^2\theta_W = 0.23$ and $\alpha = 1/128$. Since the matrix elements diverge as $p_T \to 0$, we impose a fixed p_T cut on both the jet and Higgs boson,

$$p_{Tj} = p_{TH} = p_T > 100 \text{ GeV}. \tag{2.10}$$

Both the jet and Z bosons are required to be centrally produced, with rapidity

$$|y_j| < 2.5, \qquad |y_Z| < 2.5, \tag{2.11}$$

and to be well separated from each other,

$$\cos\theta_{Zj} < 0.7, \tag{2.12}$$

where θ_{Zj} is the angle between between the Z and the jet. These cuts define a region of phase space which is both experimentally relevant and in which the matrix elements are well behaved. To illustrate the effect of the top quark mass, we show the exact p_T distribution for $m_t = 80$ GeV and 200 GeV for three representative values of the Higgs boson mass, $m_H = 250$ GeV, 500 GeV and 750 GeV. Depending on the choice for m_H, varying m_t may cause the differential cross section to change by over an order of magnitude.

We also show the p_T distributions in the large and small top quark mass approximations. Although the small mass expansion overestimates the cross section for $m_H = 250$ GeV and $m_t = 200$ GeV by a large factor, in all other cases it is a rather good approximation and lies within 20% of the exact result over the whole range of p_T. The large mass expansion, on the other hand, leads to a rather different shape of the transverse momentum distribution, and consistently overestimates the cross section at large p_T. Only for $m_H = 250$ GeV and $m_t = 200$ GeV is the large mass limit a better approximation than the small mass expansion.

As mentioned before, at large p_T, $\hat{s} \sim 4p_T^2$, and the p_T distribution becomes independent of m_H. This is illustrated in Fig. 6 where we show the transverse momentum distributions for $m_H = 250$, 500 and 750 GeV for both $m_t = 80$ GeV and in the heavy quark limit. In both cases, the p_T distributions differ at most by a factor of two at large p_T. Once again, the different shape of the large mass expansion is evident, and, for this value of m_t overshoots the exact result by a factor of 50 at $p_T \sim 1000$ GeV.

To illustrate the range of validity of the small mass expansion, in Fig. 7, we show the total cross section σ normalised to the cross section in the small quark mass limit, σ_0, as a function of m_t/m_H. Since we have taken the ratio of the cross sections, the effects of the cuts (2.10)–(2.12) tend to cancel. Furthermore, the uncertainties in the strong coupling constant also cancel. We clearly see that for all three choices of m_H, the approximation works well – to better than 10% for $m_t/m_H < 0.32$ – and only starts to break down close to the $2m_t = m_H$ threshold. For $m_H = 750$ GeV, the small mass expansion is good for top quark masses $m_t < 240$ GeV. Eventually, however, the approximation breaks down with increasing m_t and overestimates the cross section by an order of magnitude for $m_t/m_H \gtrsim 0.55$. The main reason for this sudden collapse is the fact that the threshold behaviour, which causes the exact result to suddenly diminish, has been explicitly removed. The imaginary pieces of the small mass expansion carry on growing and cause the overestimation of the cross section.

On the other hand, we see that the approximation for fixed m_t/m_H is worse for larger m_H. The total cross section is dominated by the region close to the p_T cut and, for larger m_H, this allows p_T/m_H to be small compared to m_t/m_H and causes the approximation to become worse. Increasing the p_T cut for a given value of m_H therefore improves the accuracy of the approximation. However, due to the threshold behaviour, the small mass expansion is never good for $m_t/m_H \gtrsim 0.45$.

In Fig. 8 we show the total cross section σ normalised to the cross section in the heavy quark limit, σ_∞, as a function of m_t/m_H. Figure 8a displays the results for three different values of m_H and a fixed minimum transverse momentum of $p_T > 100$ GeV for the Higgs boson. For comparison, we also show the $O(\alpha_s^2)$ cross section for centrally produced Higgs bosons normalised to the $O(\alpha_s^2)$ large mass limit. Both sets of curves exhibit similar behaviour – rapid growth at small m_t/m_H separated from the large mass region by a resonance structure due to the threshold at $2m_t = m_H$. The detailed behaviour, however, is somewhat different. The peak in the $O(\alpha_s^2)$ process decreases with increasing m_H, while the opposite is true for the $O(\alpha_s^3)$ processes. In the first case, this is due to the increasing width of the Higgs boson which smears out the resonance structure. The situation is more complicated for the $O(\alpha_s^3)$ processes since the matrix elements contain thresholds at both $2m_t = m_H$ and $2m_t = \sqrt{\hat{s}}$. The cross section, which is obtained by integrating over $\hat{s}$, is dominated by the region where the two thresholds are close together, *i.e.* small values of $\hat{s}$. For fixed p_T cut, increasing m_H decreases the minimum allowed value of $\sqrt{\hat{s}}$ in units of m_H

$$\frac{\sqrt{\hat{s}_{min}}}{m_H} = \frac{p_{Tmin}}{m_H} + \sqrt{1 + \frac{p_{Tmin}^2}{m_H^2}}\ , \tag{2.13}$$

causing the cross section to increase. Conversely, increasing the p_T cut tends to separate the two thresholds and, as shown in Fig. 8b, causes the cross section to fall. In fact, for a large enough p_T cut, the resonance structure vanishes entirely and the ratio of cross sections rises monotonically with increasing m_t/m_H.

3 Signal and Background

We now turn to a more phenomenological comparison of the large p_T Higgs boson signal with the background at high energy hadron supercolliders. When the Higgs boson decays into a pair of vector bosons, the primary background processes are,

$$q\bar{q} \to VVg, \quad \text{and} \quad qg \to VVq, \tag{3.1}$$

where $V = Z$ or W. The matrix elements for these processes including the subsequent decay of the vector bosons have recently been computed [17] using spinor techniques. It is straightforward to utilise the helicity amplitudes to compute the background rate.

As in the case for Higgs boson production at large p_T, the matrix elements for the background processes (3.1) also diverge as the transverse momentum of the vector boson pair tends to zero. For this reason, it is necessary to impose a minimum transverse momentum cut,

$$p_{Tj} = p_{TVV} > 100 \text{ GeV}. \tag{3.2}$$

However, as discussed in ref. [17], a fixed p_{Tj} cut is not, on its own, sufficient to ensure that the $2 \to 3$ cross section is a small correction to the lowest order $q\bar{q} \to VV$ process at large m_{VV}. The dominant contribution arises from the $qg \to VVq$ subprocess which contains poles in $(p_V + p_q)^2$ which are regulated by the mass of the vector boson. However, at large m_{VV}, when the energy of the vector boson is large compared to its mass, $(p_V + p_q)^2$ may become small compared to the other scales present. In this region, multiple gluon emission processes become important, and the invariant mass distribution of the vector boson pair from the $2 \to 3$ processes becomes unreliable. To control this effect, one can either increase the jet p_T cut [17] or, as we shall do here, require that the V boson and jet are well separated (see Eq. (2.12)). Due to the resonant nature of the signal, this pole is not present and the signal is relatively unaffected by this cut.

For a first look at the invariant mass distribution arising from both signal and background it is convenient to treat the vector bosons as final state particles. In Figs. 9 and 10, we compare the invariant mass distributions for ZZ and WW boson pairs arising from the production and decay of a large p_T Higgs boson with the background (3.1) for LHC and SSC energies. As in section 2, we choose three representative Higgs boson masses, $m_H = 250$, 500, 750 GeV and three values of the top quark mass, $m_t = 80$, 120 and 200 GeV. We impose the cuts of Eqs. (2.10)–(2.12) and analogous cuts on the rapidity of the W bosons, $|y_W| < 2.5$, and the W-jet separation, $\cos\theta_{Wj} < 0.7$.

The top quark plays an important role in determining the size of the signal. First of all, for $m_t \lesssim m_H/2$, increasing m_t increases the $pp \to H + j$ cross section as discussed in section 2. However, the partial width for the $H \to t\bar{t}$ decay also increases, thus decreasing the $H \to VV$ branching ratio. The net effect is still an increasing cross section with m_t provided $m_t \lesssim m_H/2$. Once the threshold is crossed, the production cross section falls due to the resonance structure in the matrix elements. This is partially compensated by an increase in the $H \to VV$ branching fraction since the $H \to t\bar{t}$ channel is no longer open.

From Figs. 9 and 10 one observes that the VVj continuum background becomes more dangerous with increasing Higgs boson mass. The signal to background ratio at the SSC ($\sqrt{s} = 40$ TeV) is clearly more favorable than at the LHC ($\sqrt{s} = 16$ TeV). For fixed m_H and m_t, the signal is much more evident in the ZZ channel than for WW. This is because, although $Br(H \to WW) \sim 2\ Br(H \to ZZ)$, the $pp \to WWj$ background is approximately one order of magnitude larger than the $pp \to ZZj$ background. The reason for this large difference lies with the rather different couplings of the W and Z bosons with the quarks within the proton, and which is already manifest in the ratio of cross sections for single W and Z production at the CERN S$p\bar{p}$S and Fermilab Tevatron, $\sigma_W/\sigma_Z \sim 3$. Once the possibility for the production of W pairs through top quark decay is also allowed, the WW

signature for Higgs bosons is even less attractive.

Increasing the hadron centre of mass energy from 16 TeV to 40 TeV increases the signal by a factor of 4 for $m_H = 250$ GeV and by a factor of 6 for $m_H = 750$ GeV. This is illustrated in Table 1 and 2, where we show the cross section for both signal and background at large p_T for LHC and SSC energies respectively. The total cross section is obtained by integrating the invariant mass distribution over an interval in m_{VV} of ± 25 GeV or $\pm\Gamma_H$ centred on m_H. For light Higgs bosons, Γ_H is small and the range of integration is determined by the experimental resolution in measuring m_{VV}, which we take to be ± 25 GeV. For heavier Higgs bosons, Γ_H is much larger than the experimental resolution, and to include all of the signal, the interval size is increased. For comparison, we also show the signal and background from the $gg \to H \to VV$ and $q\bar{q} \to VV$ processes, with the same rapidity cuts on the vector bosons. For both signal and background, the $2 \to 3$ processes are typically $10-30\%$ of the $2 \to 2$ contribution and represent an important source of gauge boson pairs at both the LHC and SSC. For example, in a typical SSC year yielding an integrated luminosity of 10^4 pb^{-1}, the number of Higgs boson events with $p_T > 100$ GeV for $m_H = 500$ GeV and $m_t = 120$ GeV is 4800 (9900) in the $ZZ\,(WW)$ modes.

Whether or not any use may be made of this relatively large event rate depends on the relative sizes of the signal and background. The precise value of the signal to background ratio depends on how the collinear and soft divergences are regulated, however, in general the signal to background ratio at large p_T is worse than in the absence of the jet. The reason for this lies in the fact that the parton-parton luminosities are strongly ordered in size, $\mathcal{L}_{gg} > \mathcal{L}_{qg} > \mathcal{L}_{q\bar{q}}$. Since the qg luminosity is much larger than that for $q\bar{q}$, the $qg \to VVq$ background is enhanced relative to the lowest order $q\bar{q} \to VV$ process. The signal, on the other hand, already samples the large gg luminosity at lowest order and does not gain such an enhancement.

So far, we have only examined the invariant mass distribution of the vector boson pair by treating the vector bosons as final state particles. In practise, the W and Z bosons must be identified through their decay products. When both of the vector bosons decay leptonically, the final state is rather clean. It either consists of four charged leptons or two charged leptons accompanied by large missing transverse momentum, $\not{p}_T$, recoiling against a large p_T jet. The branching fractions for these two all leptonic decay modes summed over both electrons and muons are $4.5 \cdot 10^{-3}$ and $4.7 \cdot 10^{-2}$ respectively, which leads to a rather small rate. Moreover, in the WW case the missing transverse momentum results from two neutrinos so that the invariant mass of the W pair cannot be reconstructed. On the other hand, if one of the vector bosons would decay hadronically, the branching fractions are then 9.4% and 29.2% respectively yielding a much larger event rate. The final state then contains either two charged leptons or one charged lepton accompanied by missing p_T, and three hadronic jets, two of which have an invariant mass close to M_V. In this case, there is an additional 'fake' background from processes of the type,

$$gg \to Vq\bar{q}g, \qquad etc. \tag{3.3}$$

where two of the jets have an invariant mass close to M_V and fake the hadronic decay of a V boson. The precise level of the 'fake' background depends on how well the invariant mass of the jet-jet system can be measured.

The invariant mass distribution of the ZZ pair for the signal, $pp \to Hj \to e^+e^-jjj$, the 'real' $pp \to ZZj \to e^+e^-jjj$ and the 'fake' $pp \to Zjjj \to e^+e^-jjj$ background at $\sqrt{s} = 40$ TeV is shown in Fig. 11. To compute the $Zjjj$ background we have used the results of refs. [18, 19]. To make an approximate detector simulation we impose the following acceptance requirements:

- One central large p_T jet j_1,

$$|y_{j_1}| < 2.5, \qquad p_{Tj_1} > 100 \text{ GeV}. \tag{3.4}$$

- Two other central jets, j_2 and j_3

$$|y_{j_i}| < 2.5, \qquad p_{Tj_i} > 25 \text{ GeV}, \qquad i = 2, 3. \tag{3.5}$$

Furthermore, the invariant mass of the two jets, $m_{j_2j_3}$ must lie within Δ of M_Z,

$$M_Z - \Delta < m_{j_2j_3} < M_Z + \Delta. \tag{3.6}$$

Typically, the invariant mass of a pair of jets can be measured with a resolution of 10%, and for our numerical simulations we have chosen $\Delta = 10$ GeV.

- A central e^+e^- pair

$$|y_e| < 2.5, \qquad p_{Te} > 25 \text{ GeV}. \tag{3.7}$$

- All jets must be well separated,

$$\cos\theta_{j_i j_j} < 0.7 \quad i,j = 1,2,3 \ . \tag{3.8}$$

- All jets and charged leptons must be well separated,

$$\cos\theta_{j_i e} < 0.7 \quad i = 1,2,3 \ . \tag{3.9}$$

The jet-jet separation cut (3.8) is necessary because collinear jets can not be separated in a detector. The cut on the electron-jet angle, (3.9), is needed to suppress backgrounds from heavy quark (c, b) decays.

The separation cuts mainly reduce the fake $Zjjj$ background by eliminating events in which at least one of the jets has a typical bremsstrahlung characteristics, *i.e.* is much softer than the other two jets and almost collinear to one of them. They have a similar effect as the jet asymmetry cut introduced in ref. [9]. However, they also reduce the signal cross section significantly and the increase in cross section due to the higher branching fraction when one Z decays hadronically is partially lost. The large reduction of the signal can be easily understood from the expected topology of an Hj event where the Higgs boson decays into a pair of Z bosons. Since the large p_T jet recoils against the Higgs boson the Z pair and also the ZZ decay products all tend to be in the same hemisphere, opposite to the jet, if the Higgs boson is not too heavy. Separation cuts between the Z decay products therefore reduce the signal cross section substantially. Of course, with increasing m_H the Z bosons become more energetic and well separated, weakening the effect of the separation cuts between the decay products of different Z bosons. In this case, however, the decay products of a given Z boson become more collinear and less well separated, resulting in a similar reduction of the signal. Relaxing the separation cut on the two jets from Z decay and observing one rather fat jet with an invariant mass close to M_Z would therefore increase the heavy Higgs signal. However, the fake $Zjjj$ background would increase even more significantly due to the collinear nature of QCD bremsstrahlung.

From Fig. 11 we observe that the signal is still evident above the real background, however, the fake background is approximately two orders of magnitude larger than the real background. In the most optimistic cases, $m_H = 250$ GeV or $m_H = 500$ GeV and $m_t = 200$ GeV, the signal lies about one order of magnitude beneath the background. The signal to background ratio can be improved by imposing a stronger rapidity cut on the ZZ decay products. A more restrictive rapidity cut would, however, also considerably reduce the signal, for $|y_e|,\ |y_{j_2}|,\ |y_{j_3}| < 1.5$, for example, by about a factor of 3. Improving the resolution on the invariant mass of the jet pair, to $\Delta = 5$ GeV for example, would reduce the fake background by approximately a factor of two while leaving the signal and the real background essentially untouched. The background is still large however, and unless an extra rejection factor, from multiplicity arguments [20] for example, can be obtained, it is unlikely that Higgs bosons produced at large p_T can be seen in this channel.

The situation for the $H \to W^+W^- \to e^\pm \nu jj$ decay is slightly more complicated due to the fact that the neutrino is not directly observed. It is then impossible to unambiguously reconstruct the invariant mass of the W pair. In this case, the cluster transverse mass,

$$m^2_{TWjj} = \left(\sqrt{m^2_{ej_2j_3} + \mathbf{p}^2_{TC}} + |\not{\mathbf{p}}_T|^2\right)^2 - \left(\mathbf{p}_{TC} + \not{\mathbf{p}}_T\right)^2 , \tag{3.10}$$

where $\mathbf{p}_{TC} = \mathbf{p}_{Te} + \mathbf{p}_{Tj_2} + \mathbf{p}_{Tj_3}$ is the cluster transverse momentum, is a more relevant quantity. In Fig. 12 we show the m_{TWjj} distribution for the signal $pp \to Hj \to W^+W^-j \to e^\pm \not{p}_T jjj$, the 'real' background $pp \to W^+W^-j \to e^\pm \not{p}_T jjj$ and the 'fake' background $pp \to W^\pm jjj \to e^\pm \not{p}_T jjj$ at the SSC. Besides the jet and lepton cuts of Eqs. (3.4)–(3.9) we apply a missing transverse momentum cut,

$$\not{p}_T > 25 \text{ GeV}, \tag{3.11}$$

and require that the $\not{p}_T$ vector must not lie close to a jet,

$$\cos\theta_{j_i \not{p}_T} < 0.7 \qquad i = 1, 2, 3 \ . \tag{3.12}$$

The last cut ensures that events where one energetic particle within a jet escapes from the detector are excluded. $m_{j_2j_3}$ now must lie within $\Delta = 10$ GeV of M_W.

The $W^\pm jjj$ background is about a factor of twenty larger than the $Zjjj$ background due mainly to the larger $Wq\bar{q}$ couplings and the larger $W \to e\nu$ branching fraction. As mentioned earlier, the 'real' background is more severe for the $H \to WW$ decay mode. Furthermore, the transverse mass distribution is less sharply peaked at m_H than the m_{WW} distribution and signal events are pushed to lower m_T. The net result is that the signal to background ratio is at best ~ 0.01. Allowing for the fact that W pairs may also be produced in top quark decay, $pp \to t\bar{t} \to W^+W^-b\bar{b}$, it would seem impossible to identify the large p_T $H \to W^+W^- \to \ell^\pm \nu q\bar{q}$ decay mode at the LHC or SSC.

4 Conclusions

The complete calculation of the transverse momentum distribution of the Higgs boson at hadron supercolliders is a formidable task. In this paper we have concentrated on the top quark mass dependence of the large p_T cross section which is dominated by the $gg \to gH$ process. A more complete description of the small p_T region requires the inclusion of both virtual and higher order corrections, and in particular the resummation of soft gluon emission [21]. Moreover, the contribution from the WW fusion process (1.2) and $pp \to t\bar{t}H$ [22] to the transverse momentum distribution of the Higgs boson must be taken into account.

We have presented two approximate forms for the $O(\alpha_s^3)$ matrix elements and investigated their domains of validity. Both approximations are somewhat simpler than the exact result and serve to highlight the mass dependence. The large mass approximation has the advantage of being extremely compact, however, it is not, in general, a faithfull representation of the exact p_T distribution. At large p_T it severely overestimates the exact result. The small mass approximation is much more accurate over the whole range of p_T, typically lying within 10% of the exact result for $m_t/m_H \lesssim 0.3$. However it is somewhat less compact and the amplitudes still contain real Spence functions.

The cross sections listed in Table 1 and 2 demonstrate that the production of Higgs bosons produced at large p_T is a significant source of Higgs bosons at future hadron supercolliders. We have investigated the observability of Higgs bosons recoiling against a large transverse momentum jet, by comparing the signal with the WWj and ZZj backgrounds at the vector boson level. In general, the signal is not improved relative to the case without the jet, and, especially for the WW signal, is marginally worse in many cases. On the other hand, the signal for Higgs bosons with mass $m_H \lesssim 500$ GeV is clearly visible above the background in the ZZ channel at the SSC, even allowing for a double charged lepton branching ratio of $4.5 \cdot 10^{-3}$. It is clear that the rate at large p_T is between 5 and 10 times smaller than the signal rate without the jet, however, the observation of a signal at large p_T would be a useful confirmation of the Higgs boson signal.

Finally, in an attempt to increase the signal rate at large p_T, we have compared the signal and background in the mixed hadronic-leptonic decay channel. In this case, the dominant background is $pp \to Vjjj$, $V = W,\ Z$, where two of the jets have an invariant mass close to M_V. In general the fake background is one to two orders of magnitude above the signal, and unless the background can be further suppressed, *e.g.* by requiring that the event have low hadronic multiplicity, it is unlikely that the large p_T Higgs boson can be seen in this channel.

Acknowledgements

We would like to thank W. Giele, J. J. van der Bij and D. Zeppenfeld for useful discussions. We also thank the authors of ref. [19] for making the matrix elements for $pp \to Vjjj$ available to us in the form of a FORTRAN program. This research was supported in part by the University of Wisconsin Research Committee with funds granted by the Wisconsin Alumni Research Foundation, and in part by the U. S. Department of Energy under contract DE-AC02-76ER00881.

A Matrix Elements

In this appendix we give analytic expressions for the squared matrix elements for the processes,

$$i(-p_1)+j(-p_2)\rightarrow k(p_3)+H(p_H)\ , \tag{A.1}$$

and,

$$i(-p_1)+j(-p_2)\rightarrow k(p_3)+H^*\rightarrow k(p_3)+V_1(p_4)+V_2(p_5)\ , \tag{A.2}$$

where $V_1V_2=WW$ or ZZ, followed by the decays,

$$V_1(p_4) \rightarrow a(p_a)+\bar{b}(p_b)\ , \tag{A.3}$$

$$V_2(p_5) \rightarrow c(p_c)+\bar{d}(p_d)\ . \tag{A.4}$$

The matrix elements for process (A.1) are given in ref. [12], however, since we use a different notation we reproduce them here.

First of all, we consider the production of an on-shell Higgs boson at large transverse momentum via the gluon fusion process,

$$gg\rightarrow gH\ , \tag{A.5}$$

shown in Fig. 1a. The unaveraged matrix elements are given by,

$$\sum\left|\mathcal{M}_{gg}(m_H^2)\right|^2=\frac{\alpha_W\alpha_s^3}{4M_W^2}\,\frac{3}{2}\left(\sum_{\lambda_1,\lambda_2,\lambda_3=\pm}\left|\sum_q\mathcal{M}_{\lambda_1\lambda_2\lambda_3}\right|^2\right), \tag{A.6}$$

where,

$$\alpha_W=\frac{g_W^2}{4\pi}=\frac{e^2}{4\pi\sin^2\theta_W}\ , \tag{A.7}$$

and,

$$\alpha_s=\frac{g_s^2}{4\pi}=\frac{12\pi}{(33-2\ N_q)\log(Q^2/\Lambda^2)}\ . \tag{A.8}$$

N_q is the effective number of quark flavors. The factor 3/2 in Eq. (A.6) results from the square of the antisymmetric structure constant $f^{abc}/4$. For a given quark of mass m_q circulating in the loop there are eight helicity amplitudes which are related by parity,

$$\mathcal{M}_{\lambda_1\lambda_2\lambda_3}=-\mathcal{M}_{-\lambda_1-\lambda_2-\lambda_3}\ . \tag{A.9}$$

The four remaining amplitudes are further related,

$$\mathcal{M}_{-+-}(s,t,u) = \mathcal{M}_{+++}(t,s,u)\,, \tag{A.10}$$

$$\mathcal{M}_{-++}(s,t,u) = \mathcal{M}_{+++}(u,t,s)\,, \tag{A.11}$$

leaving only two independent amplitudes, $\mathcal{M}_{+++}$ and $\mathcal{M}_{++-}$. To describe the two independent helicity amplitudes we make the following definitions,

$$s = (p_1+p_2)^2, \quad t = (p_2+p_3)^2, \quad u = (p_3+p_1)^2, \tag{A.12}$$

$$s_1 = s - m_H^2, \quad t_1 = t - m_H^2, \quad u_1 = u - m_H^2, \tag{A.13}$$

and,

$$\Delta = \sqrt{\frac{stu}{8}}\,. \tag{A.14}$$

We find,

$$\begin{aligned}\frac{\mathcal{M}_{+++}}{m_q^2\Delta} = &- 64\left[\frac{1}{ut}+\frac{1}{tt_1}+\frac{1}{uu_1}\right] - \frac{64}{s}\left[\frac{2s+t}{u_1^2}\,B_1(u) + \frac{2s+u}{t_1^2}\,B_1(t)\right]\\ &- \frac{16(s-4m_q^2)}{stu}\left[s_1\,C_1(s) + (u-s)\,C_1(t) + (t-s)\,C_1(u)\right]\\ &- 128m_q^2\left[\frac{1}{tt_1}\,C_1(t) + \frac{1}{uu_1}\,C_1(u)\right] + \frac{64m_q^2}{s}\,D(u,t)\\ &+ \frac{8(s-4m_q^2)}{stu}\left[st\,D(s,t) + us\,D(u,s) - ut\,D(u,t)\right] - \frac{32}{s^2}\,E(u,t)\,,\end{aligned} \tag{A.15}$$

and,

$$\begin{aligned}\frac{\mathcal{M}_{++-}}{m_q^2\Delta} = &\frac{64m_H^2}{stu} + \frac{16(m_H^2-4m_q^2)}{stu}\left[s_1\,C_1(s) + u_1\,C_1(u) + t_1\,C_1(t)\right]\\ &- \frac{8(m_H^2-4m_q^2)}{stu}\left[st\,D(s,t) + us\,D(u,s) + ut\,D(u,t)\right]\,.\end{aligned} \tag{A.16}$$

The functions B_1, C, C_1, D and E are the basic scalar integrals described in Appendix B. We have checked that these helicity amplitudes reproduce the results in ref. [12] both analytically and numerically.

The squared matrix elements for the on-shell production of a large p_T Higgs boson via the quark-antiquark annihilation process,

$$q\bar{q} \to gH, \tag{A.17}$$

shown in Fig. 1b are given by,

$$\sum \left|\mathcal{M}_{q\bar{q}}(m_H^2)\right|^2 = 16\,\alpha_s^3\alpha_W \;\frac{u^2+t^2}{s_1^2}\;\frac{1}{sM_W^2}\;|\mathcal{A}|^2 \;, \tag{A.18}$$

where,

$$\mathcal{A} = \sum_q m_q^2 \left(2 + \frac{2s}{s_1}\;B_1(s) + (4m_q^2 - u - t)\;C_1(s)\right) \;. \tag{A.19}$$

The matrix elements for the crossed processes,

$$qg \to qH \qquad \text{and} \qquad g\bar{q} \to \bar{q}H, \tag{A.20}$$

are obtained by the permutations,

$$\sum \left|\mathcal{M}_{qg}(m_H^2)\right|^2(s,t,u) = -\sum \left|\mathcal{M}_{q\bar{q}}(m_H^2)\right|^2(u,t,s) \;, \tag{A.21}$$

and,

$$\sum \left|\mathcal{M}_{g\bar{q}}(m_H^2)\right|^2(s,t,u) = -\sum \left|\mathcal{M}_{q\bar{q}}(m_H^2)\right|^2(t,s,u) \;. \tag{A.22}$$

In the limit that the quark mass is large compared to all other scales,

$$m_q^2 \gg s, t, u, m_H^2 \;, \tag{A.23}$$

the matrix elements reduce to the simple form,

$$\sum \left|\mathcal{M}_{gg}^{\infty}(m_H^2)\right|^2 \;=\; \frac{32\alpha_s^3\alpha_W}{3}\;\frac{s^4+t^4+u^4+m_H^8}{stuM_W^2} \;, \tag{A.24}$$

$$\sum \left|\mathcal{M}_{q\bar{q}}^{\infty}(m_H^2)\right|^2 \;=\; \frac{16\alpha_s^3\alpha_W}{9}\;\frac{u^2+t^2}{sM_W^2}. \tag{A.25}$$

Let us now turn to the matrix elements for the off-shell production and decay process, Eq. (A.2). Because of the scalar nature of the Higgs boson, the matrix elements factorise,

$$\sum |\mathcal{M}_{ij}|^2 = \frac{\sum |\mathcal{M}_{ij}(m_{VV}^2)|^2 \;\; \sum |\mathcal{M}_{VV}|^2}{(m_{VV}^2 - m_H^2)^2 + m_H^2\Gamma_H^2} \;, \tag{A.26}$$

where m_{VV} ($V = W,\ Z$) is the mass of the virtual Higgs boson (or equivalently, the mass of the vector boson pair), and $\sum |\mathcal{M}_{ij}(m_{VV}^2)|^2$ is obtained from the on-shell amplitudes by replacing m_H^2 with m_{VV}^2. The matrix elements for the decay,

$$H^* \to V_1 V_2 \to a\bar{b}c\bar{d}, \tag{A.27}$$

where a, b, c and d are massless fermions are given by [23]

$$\begin{aligned}\sum |\mathcal{M}_{VV}|^2 \;&=\; 16\, C_F\, g_V^6\, M_V^2\, |D_{ab}^V|^2\, |D_{cd}^V|^2 \times \\ &\left[\left(C_L^{Va2} C_L^{Vc2} + C_R^{Va2} C_R^{Vc2}\right)(p_a \cdot p_c)(p_b \cdot p_d) \;+\; \left(C_L^{Va2} C_R^{Vc2} + C_R^{Va2} C_L^{Vc2}\right)(p_b \cdot p_c)(p_a \cdot p_d)\right] .\end{aligned} \tag{A.28}$$

C_L^{Vf} and C_R^{Vf} are the usual couplings of the of the W and Z with a fermion f of charge e_f and weak isospin T_3^f,

$$C_L^{Zf} = T_3^f - e_f \sin^2\theta_W, \quad C_R^{Zf} = -e_f \sin^2\theta_W, \tag{A.29}$$

$$C_L^{Wf} = \frac{1}{\sqrt{2}}\,, \quad C_R^{Wf} = 0, \tag{A.30}$$

$g_Z = g_W / \cos\theta_W$, while the vector boson propagators are,

$$D_{ab}^V = \left[(p_a + p_b)^2 - M_V^2 + i\Gamma_V M_V\right]^{-1}. \tag{A.31}$$

The colour factor C_F counts the colour degrees of freedom of the final state,

$$C_F = 1,\ 3 \text{ or } 9, \tag{A.32}$$

for Higgs bosons decaying into 4 leptons, 2 leptons and 2 quarks and 4 quarks respectively.

B Scalar Loop Integrals

In this appendix we define the integrals appearing in the matrix elements for the $O(\alpha_s^3)$ processes for the production of a Higgs at large transverse momentum. As in the previous appendix, we use the notation,

$$s = (p_1 + p_2)^2, \quad t = (p_2 + p_3)^2, \quad u = (p_3 + p_1)^2, \tag{B.1}$$

$$s_1 = s - m_H^2, \quad t_1 = t - m_H^2, \quad u_1 = u - m_H^2. \tag{B.2}$$

First of all, the scalar two-point function $B(s)$ is given by,

$$\begin{aligned} B(s) &= -\int_0^1 dx \, \log\left(m_q^2 - i\epsilon - sx(1-x)\right) \\ &= -\left\{\log(m_q^2) - 2 + \sqrt{1 - \frac{4(m_q^2 - i\epsilon)}{s}} \, \log\left(\frac{-z}{1-z}\right)\right\} \end{aligned} \tag{B.3}$$

where,

$$z = \frac{1}{2}\left(1 + \sqrt{1 - \frac{4(m_q^2 - i\epsilon)}{s}}\right). \tag{B.4}$$

In the amplitudes only the following combination is present,

$$B_1(s) = B(s) - B(m_H^2) \, . \tag{B.5}$$

The next integral that appears is the scalar three-point function, $C(p_1, p_2)$, with two massless external lines $p_1^2 = p_2^2 = 0$, $(p_1 + p_2)^2 = s$,

$$\begin{aligned} C(s) = C(p_1, p_2) &= \frac{1}{i\pi^2} \int \frac{d^4q}{(q^2 - m_q^2)((q+p_1)^2 - m_q^2)((q+p_1+p_2)^2 - m_q^2)} \\ &= \int_0^1 \frac{dx}{sx} \, \log\left(1 - i\epsilon - \frac{s}{m_q^2} \, x(1-x)\right) \\ &= \frac{1}{2s}\left[\log\left(\frac{-z}{1-z}\right)\right]^2 \end{aligned} \tag{B.6}$$

where z is defined by Eq. (B.4). The scalar three-point function also appears with only one massless external line, $C_1(p_1, p_2) = C_1(s)$, where, $p_1^2 = 0$, $p_2^2 = m_H^2$, $(p_1 + p_2)^2 = s$, is given by,

$$s_1 C_1(s) = sC(s) - m_H^2 C(m_H^2) \, . \tag{B.7}$$

For the $gg \to gH$ process, the scalar four-point function with three massless and one massive external line, $p_1^2 = p_2^2 = p_3^2 = 0$ and $p_4^2 = m_H^2$, also appears,

$$\begin{aligned} D(s,t) &= D(p_1, p_2, p_3) \\ &= \frac{1}{i\pi^2} \int \frac{d^4q}{(q^2 - m_q^2)((q+p_1)^2 - m_q^2)((q+p_1+p_2)^2 - m_q^2)((q-p_4)^2 - m_q^2)} \end{aligned}$$

$$= \frac{1}{st}\int_0^1 \frac{dx}{x(1-x)+m_q^2u/ts}\Big\{-\log\Big(1-i\epsilon-\frac{m_H^2}{m_q^2}\,x(1-x)\Big) \tag{B.8}$$

$$+\log\Big(1-i\epsilon-\frac{s}{m_q^2}\,x(1-x)\Big)+\log\Big(1-i\epsilon-\frac{t}{m_q^2}\,x(1-x)\Big)\Big\}\,.$$

This result can be expressed in terms of complex Spence functions via the relation,

$$\int_0^1 \frac{dx}{x(1-x)+m_q^2u/ts}\ \log\Big(1-i\epsilon-\frac{v}{m_q^2}\,x(1-x)\Big)$$

$$= \frac{2}{\sqrt{1+4m_q^2u/ts}}\left\{Sp\left(\frac{x_-}{x_--y}\right)-Sp\left(\frac{x_+}{x_+-y}\right)+Sp\left(\frac{x_-}{y-x_+}\right)-Sp\left(\frac{x_+}{y-x_-}\right)\right. \tag{B.9}$$

$$\left.+\log\left(\frac{-x_-}{x_+}\right)\ \log\left(1-i\epsilon-\frac{v}{m_q^2}\,x_-x_+\right)\right\}$$

where,

$$x_\pm = \frac{1}{2}\left(1\pm\sqrt{1+\frac{4m_q^2u}{ts}}\right)\ , \tag{B.10}$$

and,

$$y = \frac{1}{2}\left(1+\sqrt{1-\frac{4(m_q^2-i\epsilon)}{v}}\right)\ . \tag{B.11}$$

Finally, as an auxiliary function we define,

$$E(u,t) = uC(u)+tC(t)+u_1C_1(u)+t_1C(t)-utD(u,t)\ . \tag{B.12}$$

C Small Quark Mass Limit

In this appendix we make an explicit expansion of the integrals defined in Appendix B in the limit that the quark mass is smaller that all other quantities,

$$m_q^2 = \mu^2 \ll p_T^2, m_H^2, s, |t|, |u|\ \text{ etc..} \tag{C.1}$$

In this limit the two point function, $B_1(x)$, is given by,

$$B_1(x) = -\log\left(\frac{|x|}{m_H^2}\right)+i\pi\Big(\theta(x)-1\Big), \tag{C.2}$$

where,

$$\theta(x) = \begin{cases} 1, & x>0, \\ 0, & x<0. \end{cases} \tag{C.3}$$

The three point functions, $C(x)$ (and hence $C_1(x)$), are then,

$$C(x) = \frac{1}{2x}\left(\log^2\left(\frac{\mu^2}{|x|}\right) - \theta(x)\left\{\pi^2 - 2i\pi\log\left(\frac{\mu^2}{|x|}\right)\right\}\right). \tag{C.4}$$

Finally, the four point functions, $D(u,t)$ and $D(s,t)$, are given by,

$$\begin{aligned} D(u,t) = \frac{1}{ut}\Bigg\{ & -2Sp\left(\frac{u_1}{u}\right) - 2Sp\left(\frac{t_1}{t}\right) + \log^2\left(-\frac{\mu^2}{u}\right) + \log^2\left(-\frac{\mu^2}{t}\right) - \log^2\left(\frac{\mu^2}{m_H^2}\right) \\ & + \frac{2\pi^2}{3} + 2\log\left(\frac{u}{t_1}\right)\log\left(\frac{t}{t_1}\right) + 2\log\left(\frac{t}{u_1}\right)\log\left(\frac{u}{u_1}\right) \\ & - \log^2\left(\frac{t_1}{u_1}\right) - \log^2\left(\frac{ut}{u_1 t_1}\right) - 2i\pi\log\left(\frac{\mu^2 t_1^2 u_1^2}{m_H^2 u^2 t^2}\right)\Bigg\}, \end{aligned} \tag{C.5}$$

and,

$$\begin{aligned} D(s,t) = \frac{1}{st}\Bigg\{ & 2\,Sp\left(\frac{t}{t_1}\right) - 2Sp\left(\frac{s_1}{s}\right) + \log^2\left(\frac{\mu^2}{s}\right) + \log^2\left(-\frac{\mu^2}{t}\right) - \log^2\left(\frac{\mu^2}{m_H^2}\right) \\ & + 2\log\left(-\frac{s}{t_1}\right)\log\left(-\frac{t}{s}\right) + \log^2\left(-\frac{t_1}{s}\right) + 2i\pi\log\left(-\frac{m_H^2}{t_1}\right)\Bigg\}. \end{aligned} \tag{C.6}$$

$D(s,u)$ is obtained by exchanging u and t in Eq. (C.6).

References

[1] M. Drees *et al.*, Proceedings of the Workshop Z Physics at LEP 1, CERN 89-08, Vol. 2, p. 58 (1989), and references therein.

[2] S. L. Wu *et al.*, Proc. ECFA workshop on LEP200, Vol. 2 (Aachen, Germany 1986), p. 312.

[3] J. F. Gunion, G. L. Kane and J. Wudka, Nucl. Phys. **B299** (1988) 231.

[4] R. N. Cahn *et al.*, Proceedings of the Workshop on Experiments, Detectors and Experimental Areas for the SSC, Berkeley, 1987, p. 20;
D. Froidevaux, Proceedings of the Workshop on Physics Physics at Future Accelerators, La Thuile (Italy) and Geneva (Switzerland), 1987, CERN 87-07, Vol. 1, p. 61.

[5] V. Barger, T. Han and R. J. N. Phillips, Phys. Rev. **D36** (1987) 295, Phys. Rev. **D37** (1988) 2005, Phys. Lett. **206B** (1988) 339.

[6] H. Georgi, S. L. Glashow, M. E. Mahacek and D. V. Nanopoulos, Phys. Rev. Lett. **40** (1978) 692.

[7] R. N. Cahn and S. Dawson, Phys. Lett. **136B** (1984) 196; **138B** (1984) 464(E),
S. Dawson, Nucl. Phys. **B249** (1984) 42.

[8] F. Abe *et al.* (CDF Collaboration), preprint UPR-0172E (1989).

[9] R. Kleiss and W. J. Stirling, Phys. Lett. **200B** (1988) 193.

[10] R. N. Cahn, S. D. Ellis, R. Kleiss and W. J. Stirling, Phys. Rev. **D35** (1987) 1626.

[11] D. A. Dicus, Chung Kao and W. W. Repko, Phys. Rev. **D36** (1987) 1570,
E. W. N. Glover and J. J. van der Bij, Nucl. Phys. **B321** (1989) 561.

[12] R. K. Ellis, I. Hinchliffe, M. Soldate and J. J. van der Bij, Nucl. Phys. **B297** (1988) 221.

[13] G. Passarino and M. Veltman, Nucl. Phys. **B160** (1979) 151.

[14] G. 't Hooft and M. Veltman, Nucl. Phys. **B153** (1979) 365.

[15] P. Langacker, Phys. Rev. Lett. **63** (1989) 1920.

[16] D. W. Duke and J. F. Owens, Phys. Rev. **D30** (1984) 49.

[17] U. Baur, E. W. N. Glover and J. J. van der Bij, Nucl. Phys. **B318** (1989) 106.

[18] K. Hagiwara and D. Zeppenfeld, Nucl. Phys. **B313** (1988) 560;
F. A. Berends, W. Giele and H. Kuijf, Nucl. Phys. **B321** (1989) 39.

[19] V. Barger, T. Han, J. Ohnemus and D. Zeppenfeld, Phys. Rev. Lett. **62** (1989) 1971, and Phys. Rev. **D40** (1989) 2888;
F. A. Berends, W. T. Giele, R. Kleiss, H. Kuijf and W. J. Stirling, Phys. Lett. **224B** (1989) 237.

[20] J. F. Gunion *et al.*, Phys. Rev. **D40** (1989) 2223.

[21] I. Hinchliffe and S. F. Novaes, Phys. Rev. **D38** (1988) 3475.

[22] Z. Kunszt, Nucl. Phys. **B247** (1984) 339.

[23] E. W. N. Glover, J. Ohnemus and S. S. D. Willenbrock, Phys. Rev. **D37** (1988) 3193.

Table 1

Cross section (in pb) for $pp \to VV$ and $pp \to VVj$ ($V = W,\ Z$) production in pp collisions at $\sqrt{s} = 16$ TeV. We show the signal from the Higgs boson and, in brackets, the background. Both vector bosons are required to have rapidity, $|y_V| < 2.5$, while the jet in the $2 \to 3$ case has rapidity $|y_j| < 2.5$ and transverse momentum $p_{Tj} > 100$ GeV. Furthermore, the jet is well separated from the vector bosons, $\cos\theta_{Vj} < 0.7$.

process	m_t [GeV]	$m_H = 250$ GeV	$m_H = 500$ GeV	$m_H = 750$ GeV
ZZ	80	4.2 (2.0)	0.23 (0.36)	0.03 (0.28)
	120	5.8 (2.0)	0.54 (0.38)	0.085 (0.30)
	200	2.8 (2.0)	1.14 (0.38)	0.24 (0.35)
ZZj	80	0.30 (0.14)	0.035 (0.058)	0.007 (0.058)
	120	0.50 (0.14)	0.085 (0.062)	0.019 (0.062)
	200	0.37 (0.14)	0.19 (0.063)	0.054 (0.070)
WW	80	9.8 (9.3)	0.47 (1.9)	0.064 (1.4)
	120	13.5 (9.3)	1.11 (2.0)	0.17 (1.6)
	200	6.5 (9.3)	2.37 (2.0)	0.49 (1.8)
WWj	80	0.69 (1.3)	0.072 (0.42)	0.014 (0.40)
	120	1.14 (1.3)	0.18 (0.44)	0.038 (0.42)
	200	0.89 (1.3)	0.39 (0.45)	0.11 (0.48)

Table 2

Cross section (in pb) for $pp \to VV$ and $pp \to VVj$ ($V = W,\ Z$) production in pp collisions at $\sqrt{s} = 40$ TeV. We show the signal from the Higgs boson and, in brackets, the background. Both vector bosons are required to have rapidity, $|y_V| < 2.5$, while the jet in the $2 \to 3$ case has rapidity $|y_j| < 2.5$ and transverse momentum $p_{Tj} > 100$ GeV. Furthermore, the jet is well separated from the vector bosons, $\cos\theta_{Vj} < 0.7$.

process	m_t [GeV]	$m_H = 250$ GeV	$m_H = 500$ GeV	$m_H = 750$ GeV
ZZ	80	16.3 (4.2)	1.1 (0.84)	0.19 (0.71)
	120	22.4 (4.2)	2.6 (0.87)	0.52 (0.77)
	200	10.7 (4.2)	5.6 (0.88)	1.46 (0.89)
ZZj	80	1.4 (0.41)	0.19 (0.20)	0.05 (0.22)
	120	2.3 (0.41)	0.48 (0.22)	0.13 (0.23)
	200	1.8 (0.41)	1.1 (0.22)	0.38 (0.27)
WW	80	37.5 (18.9)	2.3 (4.2)	0.39 (3.4)
	120	51.6 (18.9)	5.4 (4.4)	1.1 (3.8)
	200	24.6 (18.9)	11.6 (4.5)	3.0 (4.4)
WWj	80	3.1 (4.1)	0.40 (1.5)	0.094 (1.5)
	120	5.2 (4.1)	0.99 (1.6)	0.26 (1.6)
	200	4.1 (4.1)	2.2 (1.6)	0.77 (1.8)

Figure Captions

Fig. 1: The Feynman graphs contributing to the processes (a) $gg \to gH$, (b) $qg \to Hq$ and (c) $q\bar{q} \to gH$.

Fig. 2: The squared matrix elements, $|\mathcal{M}|^2$, evaluated at $\hat{s} = 4m_H^2$ and $\hat{u} = \hat{t}$ for (a) $gg \to gH$, (b) $qg \to qH$ and (c) $q\bar{q} \to gH$ as a function of m_t/m_H. The figures are normalised to the squared matrix elements for infinitely heavy top quarks, $|\mathcal{M}_\infty|^2$.

Fig. 3: The squared matrix elements for the $gg \to gH$ process evaluated at $\hat{u} = \hat{t} = (m_H^2 - \hat{s})/2$ as a function of p_T/m_t normalised (a) to the squared matrix element $|\mathcal{M}_\infty|^2$ in the limit $m_t \to \infty$ and (b) to the squared matrix element $|\mathcal{M}_0|^2$ in the small top quark mass limit for $m_H/m_t = 0.1$, 0.4, 1, 2.5 and 10.

Fig. 4: The matrix elements for the process $gg \to gH$ evaluated at $\hat{s} = 4m_H^2$ as a function of the jet centre of mass rapidity, y_j^*, for various values of m_H/m_t, normalised (a) to the squared matrix element $|\mathcal{M}_\infty|^2$ in the limit $m_t \to \infty$ and (b) to the squared matrix element $|\mathcal{M}_0|^2$ in the small top quark mass limit.

Fig. 5: The transverse momentum distribution, $d\sigma/dp_T$ for the process $pp \to Hj \to ZZj$ for pp collisions at $\sqrt{s} = 40$ TeV for (a) $m_H = 250$ GeV, (b) $m_H = 500$ GeV and (c) $m_H = 750$ GeV. The solid curves show the exact results for $m_t = 80$ GeV and 200 GeV, while the small mass approximation is shown dotted. The transverse momentum distribution in the large m_t limit is given by the dashed curve. The cuts imposed are summarized in Eqs. (2.10)–(2.12).

Fig. 6: The transverse momentum distribution, $d\sigma/dp_T$ for the process $pp \to Hj \to ZZj$ for pp collisions at $\sqrt{s} = 40$ TeV for $m_H = 250$ GeV (top), 500 GeV (middle) and 750 GeV (bottom). The solid curves show the exact result for $m_t = 80$ GeV while the large m_t approximation is shown dashed. The cuts imposed are summarized in Eqs. (2.10)–(2.12).

Fig. 7: The total cross section σ for Higgs boson production at large transverse momentum, $p_T > 100$ GeV, versus m_t/m_H for pp collisions at $\sqrt{s} = 40$ TeV as a function of m_t/m_H normalised to the cross section in the small quark mass limit, σ_0, for $m_H = 250$, 500 and 750 GeV.

Fig. 8: (a) The total cross section σ for Higgs boson production at both small transverse momentum, $p_T \sim 0$, via the $O(\alpha_s^2)$ process $gg \to H$ (upper solid, dashed and dotted curve) and at large transverse momentum, $p_T > 100$ GeV (lower solid, dashed and dotted curve) for pp collisions at $\sqrt{s} = 40$ TeV as a function of m_t/m_H normalised to the cross section in the large quark mass limit, σ_∞, for $m_H = 250$, 500 and 750 GeV.

(b) σ/σ_∞ for Higgs boson production at large transverse momentum for $m_H = 500$ GeV in pp collisions at $\sqrt{s} = 40$ TeV as a function of m_t/m_H for $p_T > 100$, 300 and 500 GeV.

Fig. 9: The invariant mass distribution, $d\sigma/dm_{ZZ}$ for both the signal $pp \to Hj \to ZZj$ and background $pp \to ZZj$ (dashed line) at (a) $\sqrt{s} = 16$ TeV and (b) $\sqrt{s} = 40$ TeV. We show results for three representative Higgs boson masses, $m_H = 250$, 500 and 750 GeV and three representative values of the top quark mass, $m_t = 80$ (solid), 120 (dotted) and 200 GeV (dot-dashed).

Fig. 10: The invariant mass distribution, $d\sigma/dm_{WW}$ for both the signal $pp \to Hj \to WWj$ and background $pp \to WWj$ (dashed line) at (a) $\sqrt{s} = 16$ TeV and (b) $\sqrt{s} = 40$ TeV. We show results for three representative Higgs boson masses, $m_H = 250$, 500 and 750 GeV and three representative values of the top quark mass, $m_t = 80$ (solid), 120 (dotted) and 200 GeV (dot-dashed).

Fig. 11: The invariant mass distribution, $B \cdot d\sigma/dm_{Zjj}$ for the signal $pp \to Hj \to ZZj \to e^+e^-jjj$, the real background $pp \to ZZj \to e^+e^-jjj$ (dashed line) and the fake background $pp \to Zjjj \to e^+e^-jjj$ (solid line) at $\sqrt{s} = 40$ TeV. We show results for three representative Higgs boson masses, $m_H = 250$, 500 and 750 GeV and three representative values of the top quark mass, $m_t = 80$ (solid), 120 (dotted) and 200 GeV (dot-dashed). B generically denotes the branching fraction: $B = 0.047$ for $ZZ \to e^+e^-jj$ and $B = 0.033$ for $Z \to e^+e^-$. The cuts imposed are described in the text.

Fig. 12: The cluster transverse mass distribution, $B \cdot d\sigma/dm_{TWjj}$ for the signal $pp \to Hj \to W^+W^-j \to e^\pm\nu jjj$, the real background $pp \to W^+W^-j \to e^\pm\nu jjj$ (dashed line) and the fake background $pp \to W^\pm jjj \to e^\pm\nu jjj$ (solid line) at $\sqrt{s} = 40$ TeV. We show results for three representative Higgs boson masses, $m_H = 250$, 500 and 750 GeV and three representative values of the top quark mass, $m_t = 80$ (solid),

120 (dotted) and 200 GeV (dot-dashed). B generically denotes the branching fraction: $B = 0.146$ for $W^+W^- \rightarrow e^\pm \nu jj$ and $B = 0.108$ for $W \rightarrow e\nu$. The cuts imposed are described in the text.

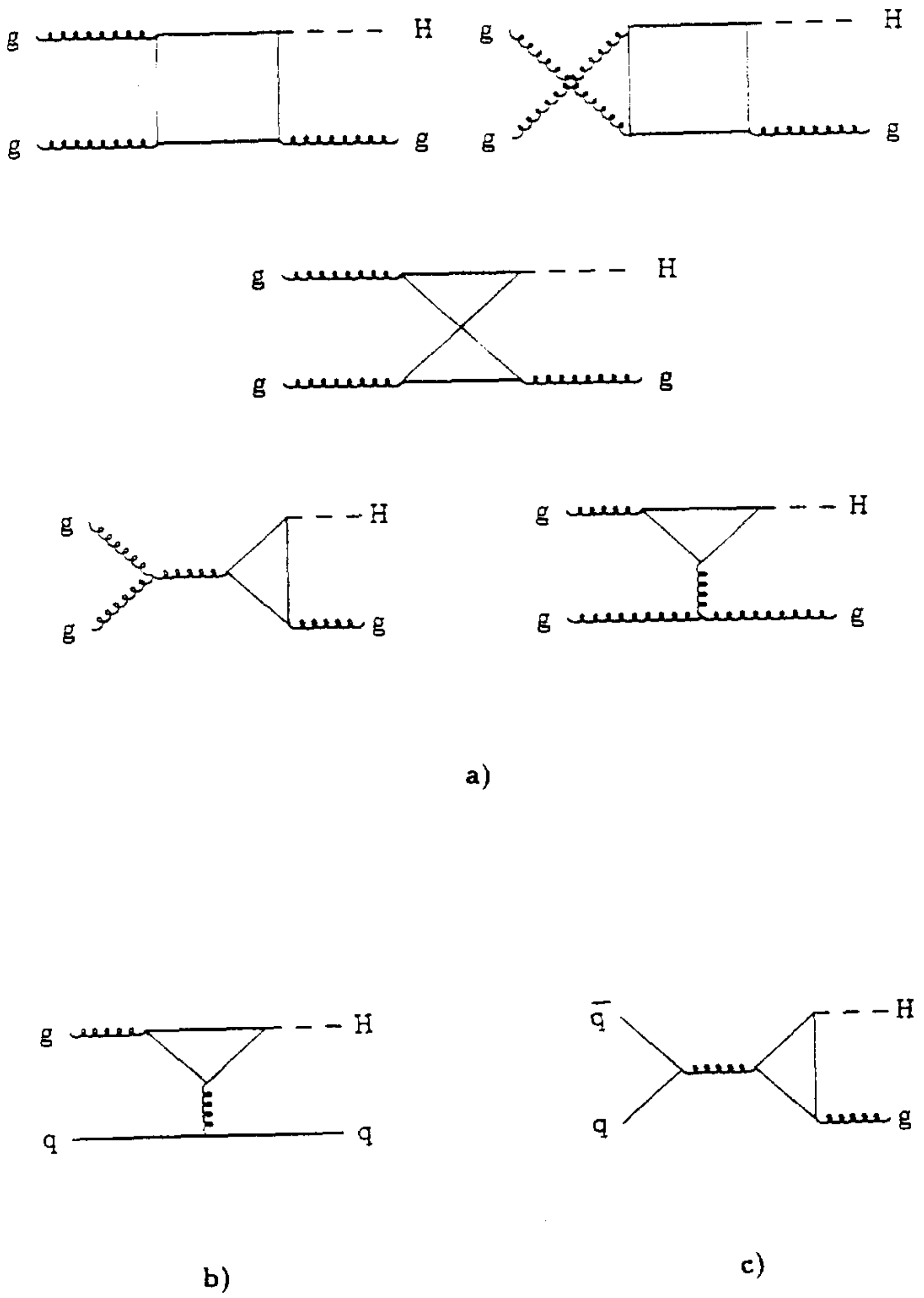

a)

b)

c)

Fig. 1

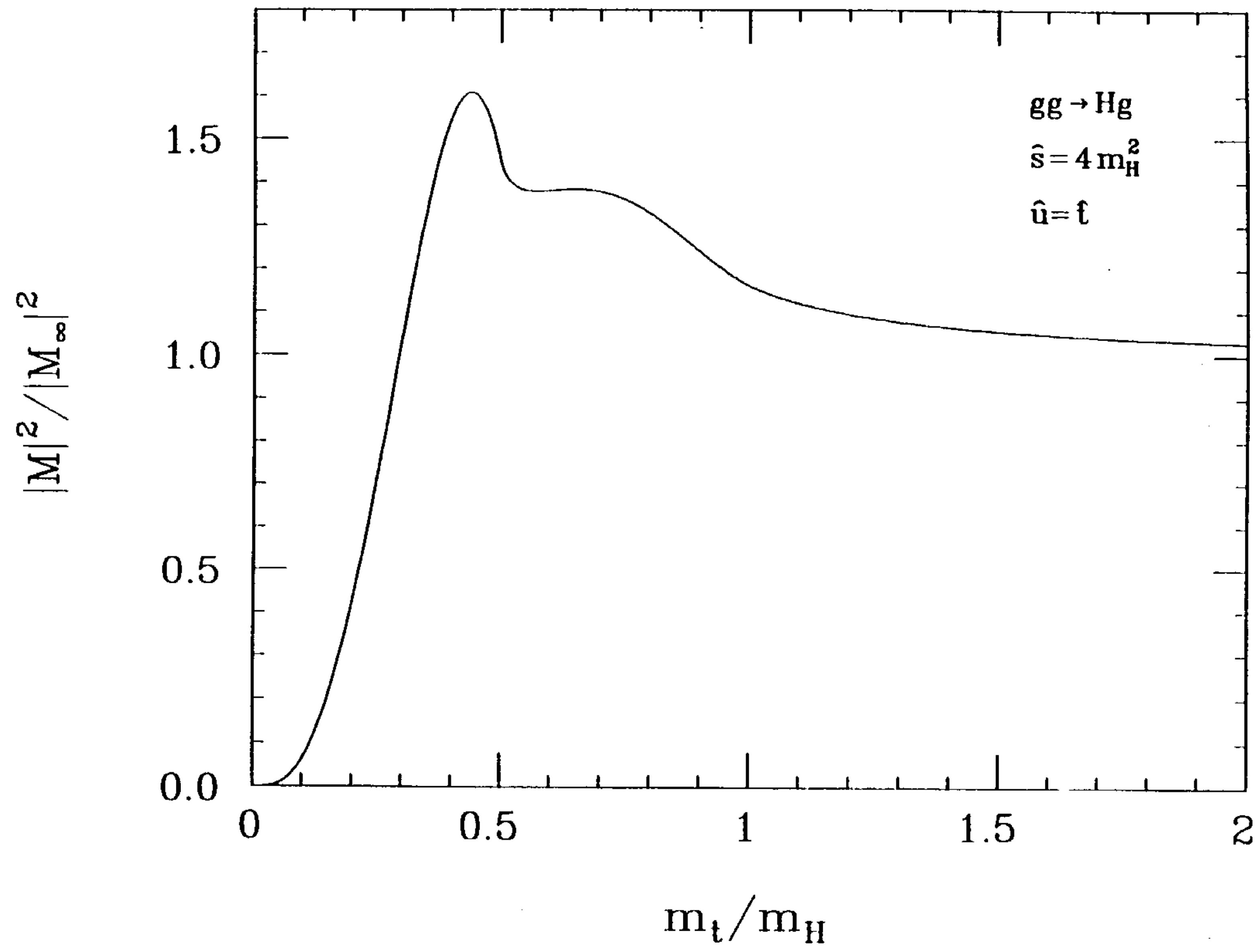

$gg \to Hg$
$\hat{s} = 4\,m_H^2$
$\hat{u} = \hat{t}$
$|M|^2/|M_\infty|^2$
0.0
0.5
1.0
1.5
0
0.5
1
1.5
2
m_t/m_H

Fig. 2a

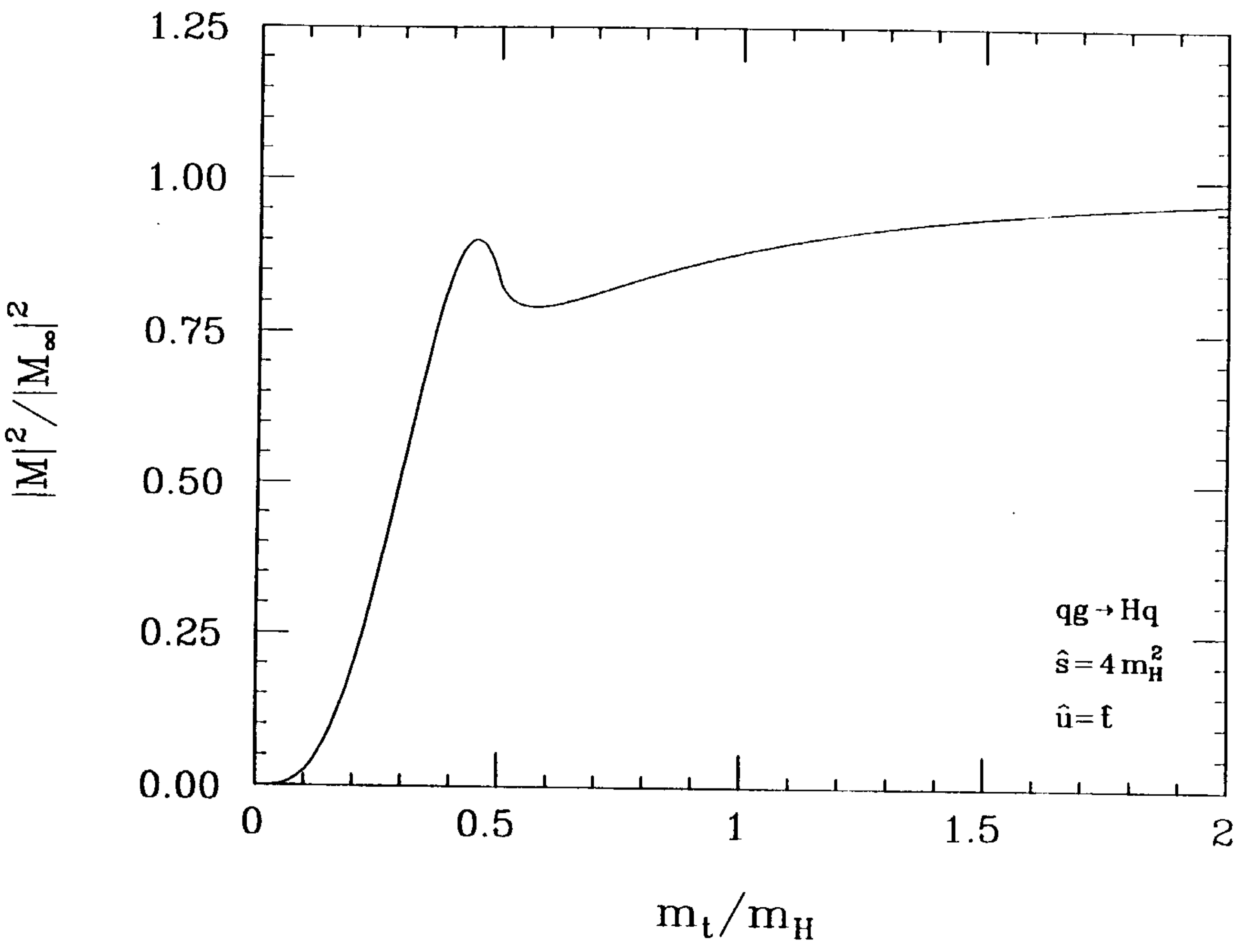
1.25
1.00
0.75
0.50
0.25
0.00
$|M|^2/|M_\infty|^2$
0
0.5
1
1.5
2
m_t/m_H
$qg \to Hq$
$\hat{s} = 4\,m_H^2$
$\hat{u} = \hat{t}$

Fig. 2b

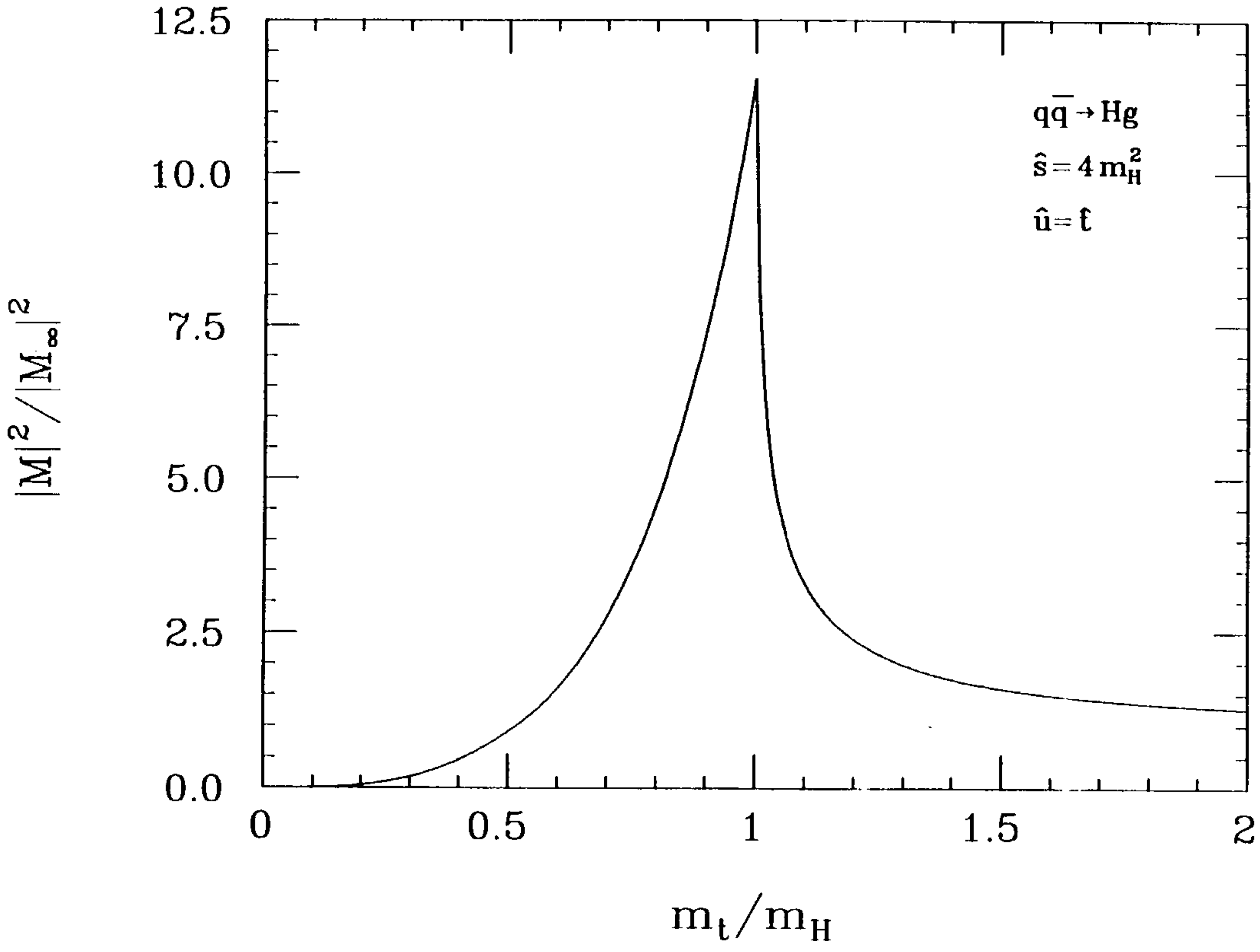
12.5
10.0
7.5
5.0
2.5
0.0
$|M|^2/|M_\infty|^2$
0
0.5
1
1.5
2
m_t/m_H
$q\bar{q} \to Hg$
$\hat{s} = 4\,m_H^2$
$\hat{u} = \hat{t}$

Fig. 2c

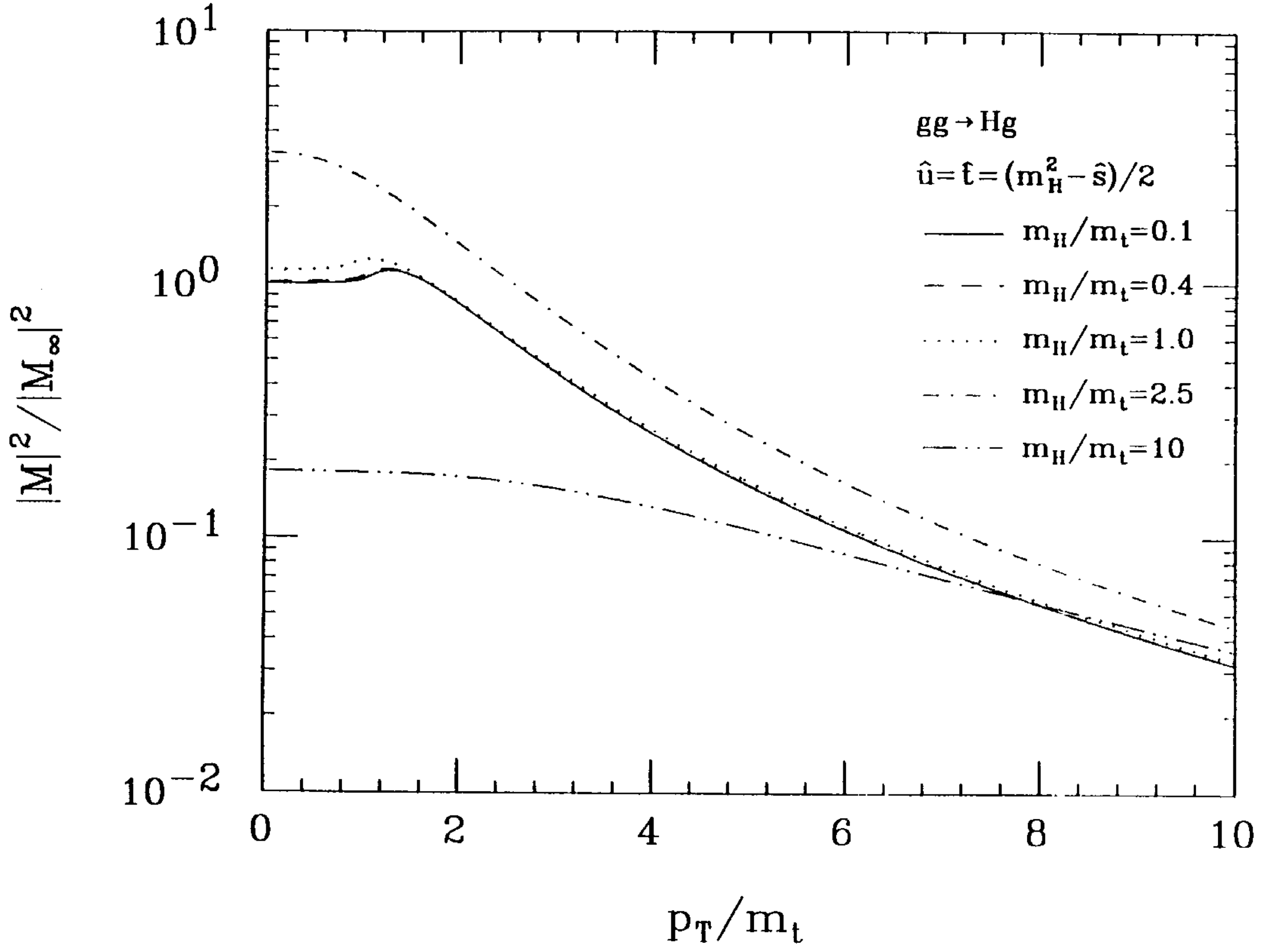
10^1
10^0
10^{-1}
10^{-2}
$|M|^2/|M_\infty|^2$
0
2
4
6
8
10
p_T/m_t
$gg \to Hg$
$\hat{u}=\hat{t}=(m_H^2-\hat{s})/2$
$m_H/m_t=0.1$
$m_H/m_t=0.4$
$m_H/m_t=1.0$
$m_H/m_t=2.5$
$m_H/m_t=10$

Fig. 3a

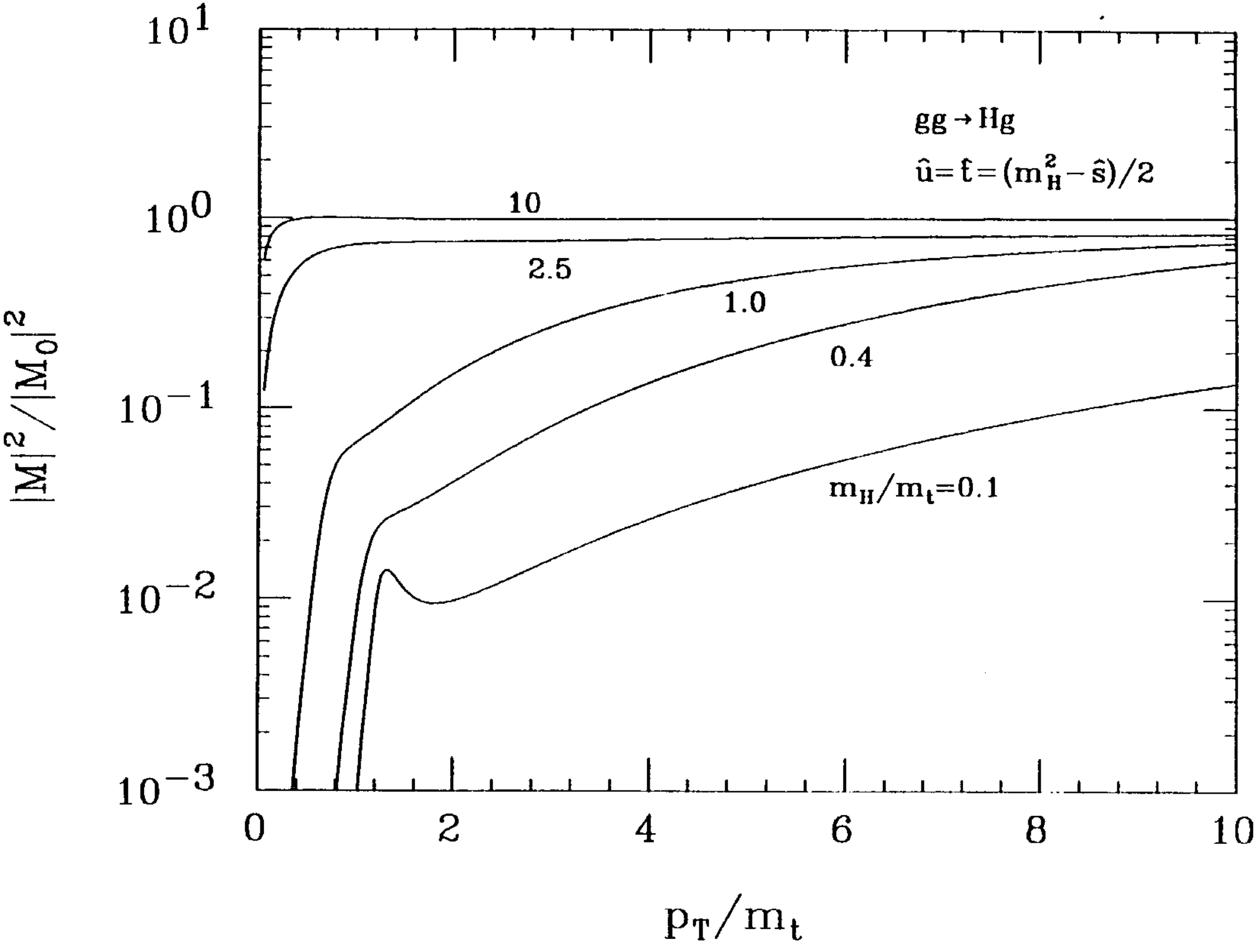
gg → Hg
$\hat{u}=\hat{t}=(m_H^2-\hat{s})/2$
10
2.5
1.0
0.4
$m_H/m_t=0.1$
10^1
10^0
10^{-1}
10^{-2}
10^{-3}
$|M|^2/|M_0|^2$
0
2
4
6
8
10
p_T/m_t

Fig. 3b

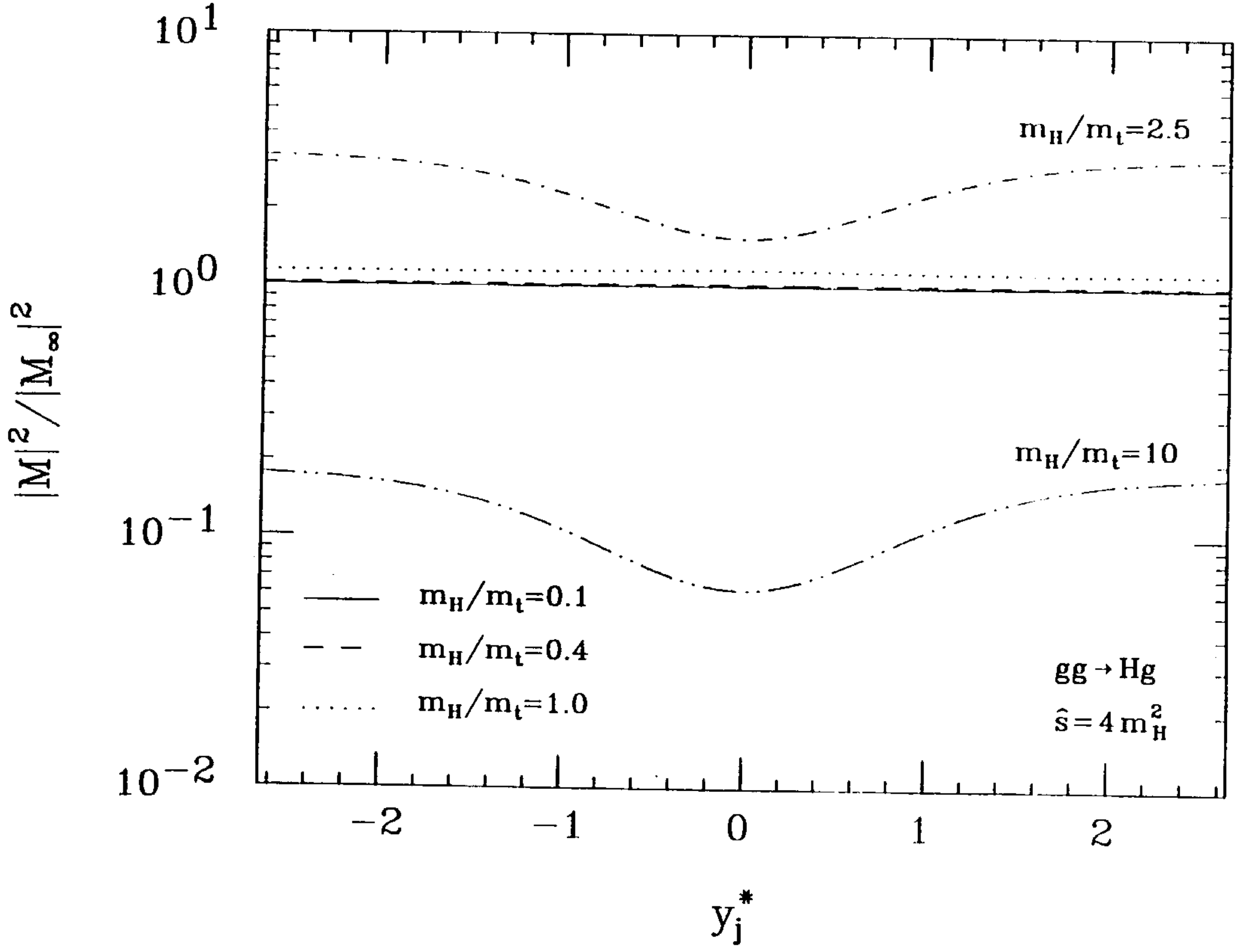
10^1
10^0
10^{-1}
10^{-2}
$|M|^2/|M_\infty|^2$
$m_H/m_t=2.5$
$m_H/m_t=10$
$m_H/m_t=0.1$
$m_H/m_t=0.4$
$m_H/m_t=1.0$
$gg \to Hg$
$\hat{s}=4\,m_H^2$
−2
−1
0
1
2
y_j^*

Fig. 4a

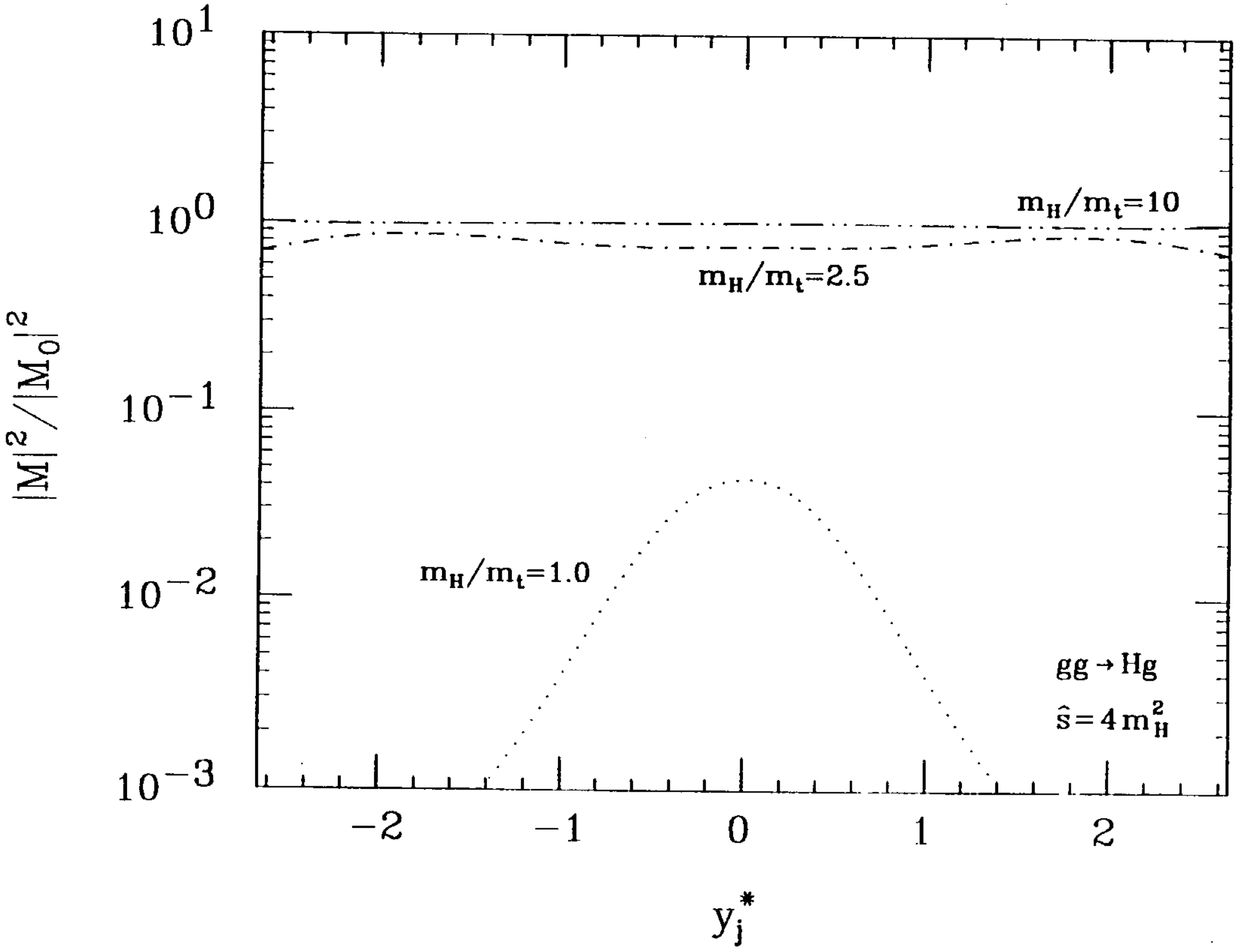
10^1
10^0
10^{-1}
10^{-2}
10^{-3}
$|M|^2/|M_0|^2$
-2
-1
0
1
2
y_j^*
$m_H/m_t=10$
$m_H/m_t=2.5$
$m_H/m_t=1.0$
$gg \to Hg$
$\hat{s}=4\,m_H^2$

Fig. 4b

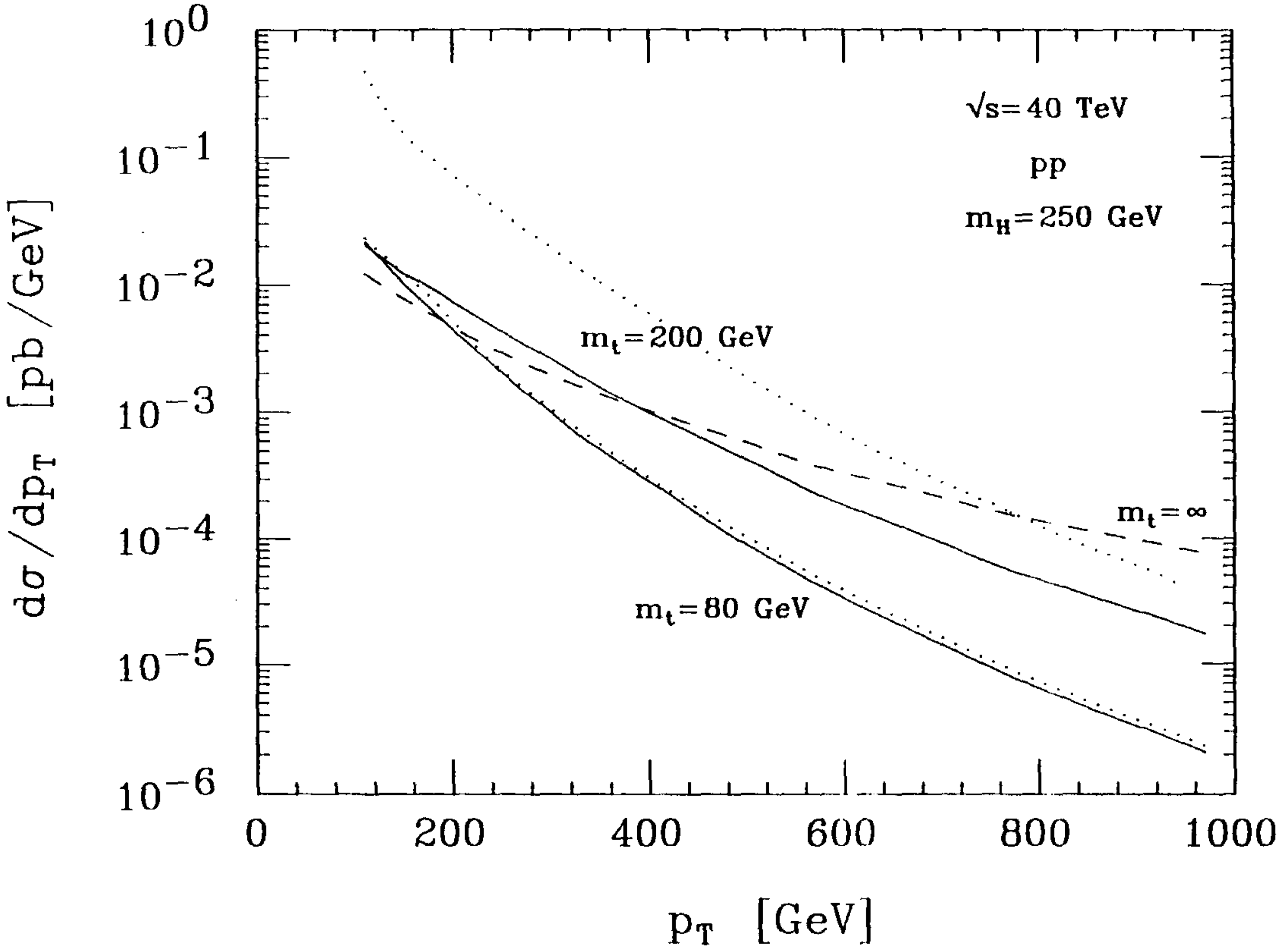
$d\sigma/dp_T$ [pb/GeV]
10^0
10^{-1}
10^{-2}
10^{-3}
10^{-4}
10^{-5}
10^{-6}
0
200
400
600
800
1000
p_T [GeV]
$\sqrt{s}=40$ TeV
pp
$m_H=250$ GeV
$m_t=200$ GeV
$m_t=\infty$
$m_t=80$ GeV

Fig. 5a

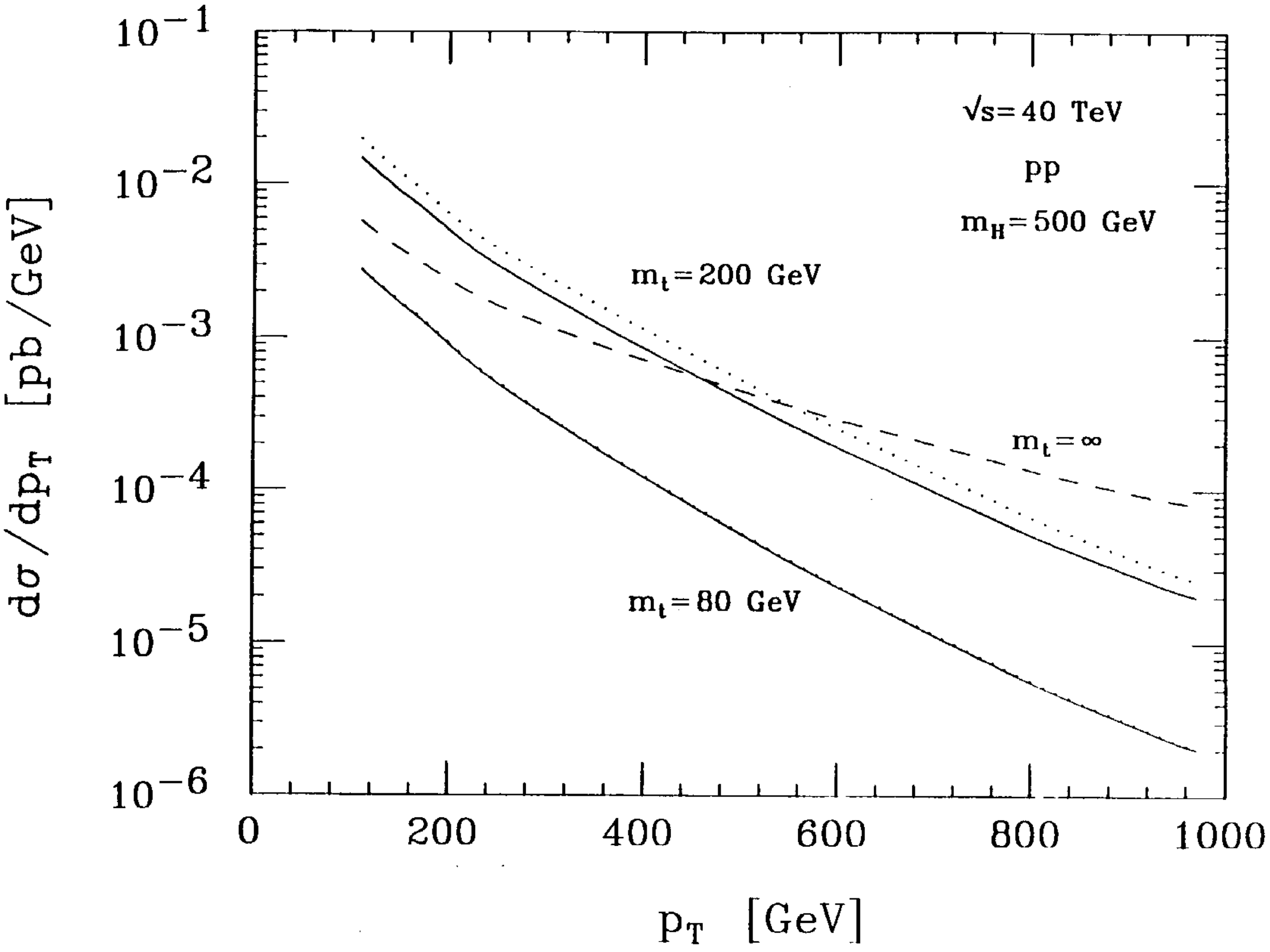
$d\sigma/dp_T$ [pb/GeV]
10^{-1}
10^{-2}
10^{-3}
10^{-4}
10^{-5}
10^{-6}
0
200
400
600
800
1000
p_T [GeV]
$\sqrt{s}=40$ TeV
pp
$m_H=500$ GeV
$m_t=200$ GeV
$m_t=\infty$
$m_t=80$ GeV

Fig. 5b

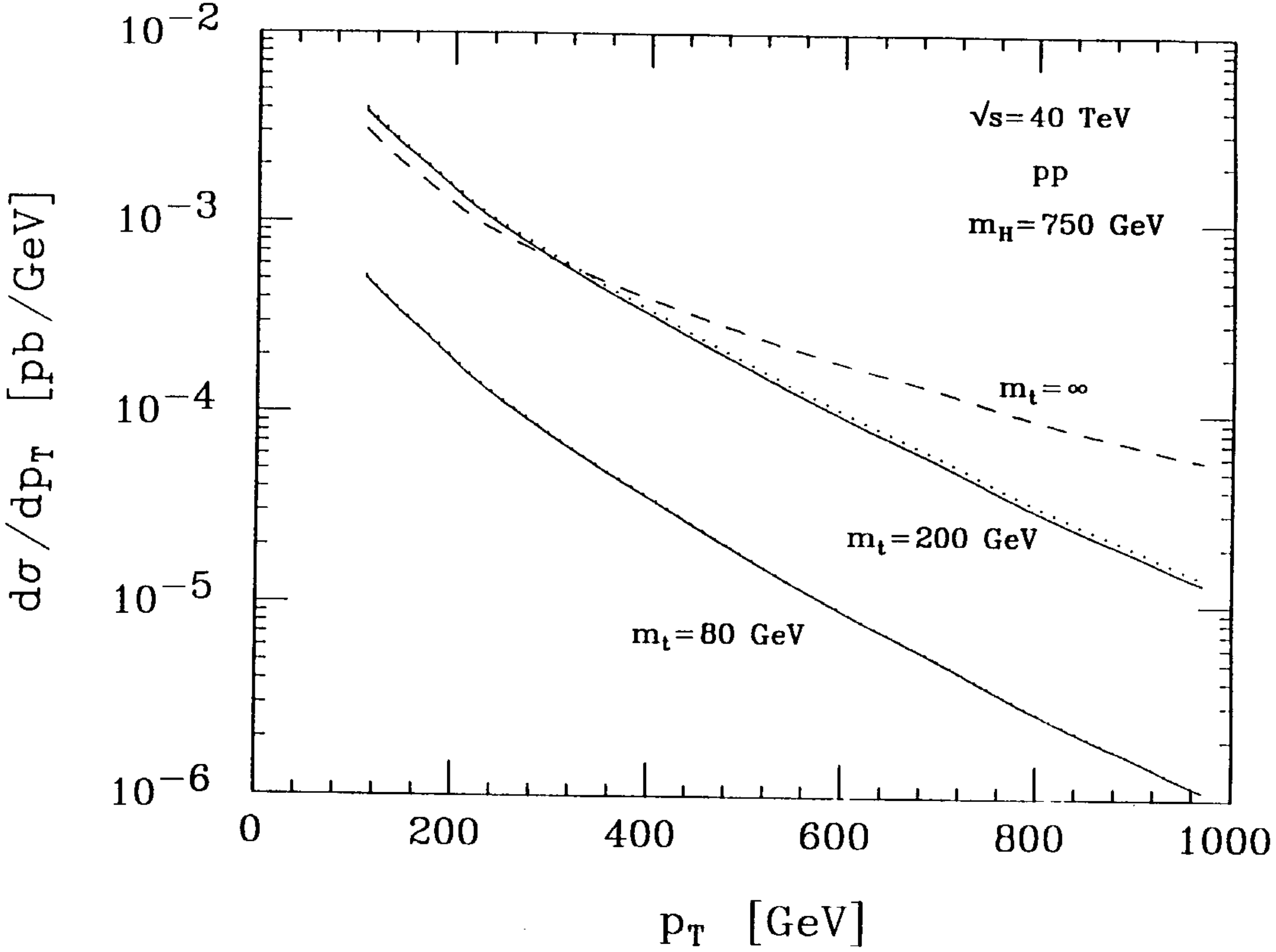
10^{-2}
10^{-3}
10^{-4}
10^{-5}
10^{-6}
$d\sigma/dp_T$ [pb/GeV]
0
200
400
600
800
1000
p_T [GeV]
$\sqrt{s}=40$ TeV
pp
$m_H=750$ GeV
$m_t=\infty$
$m_t=200$ GeV
$m_t=80$ GeV

Fig. 5c

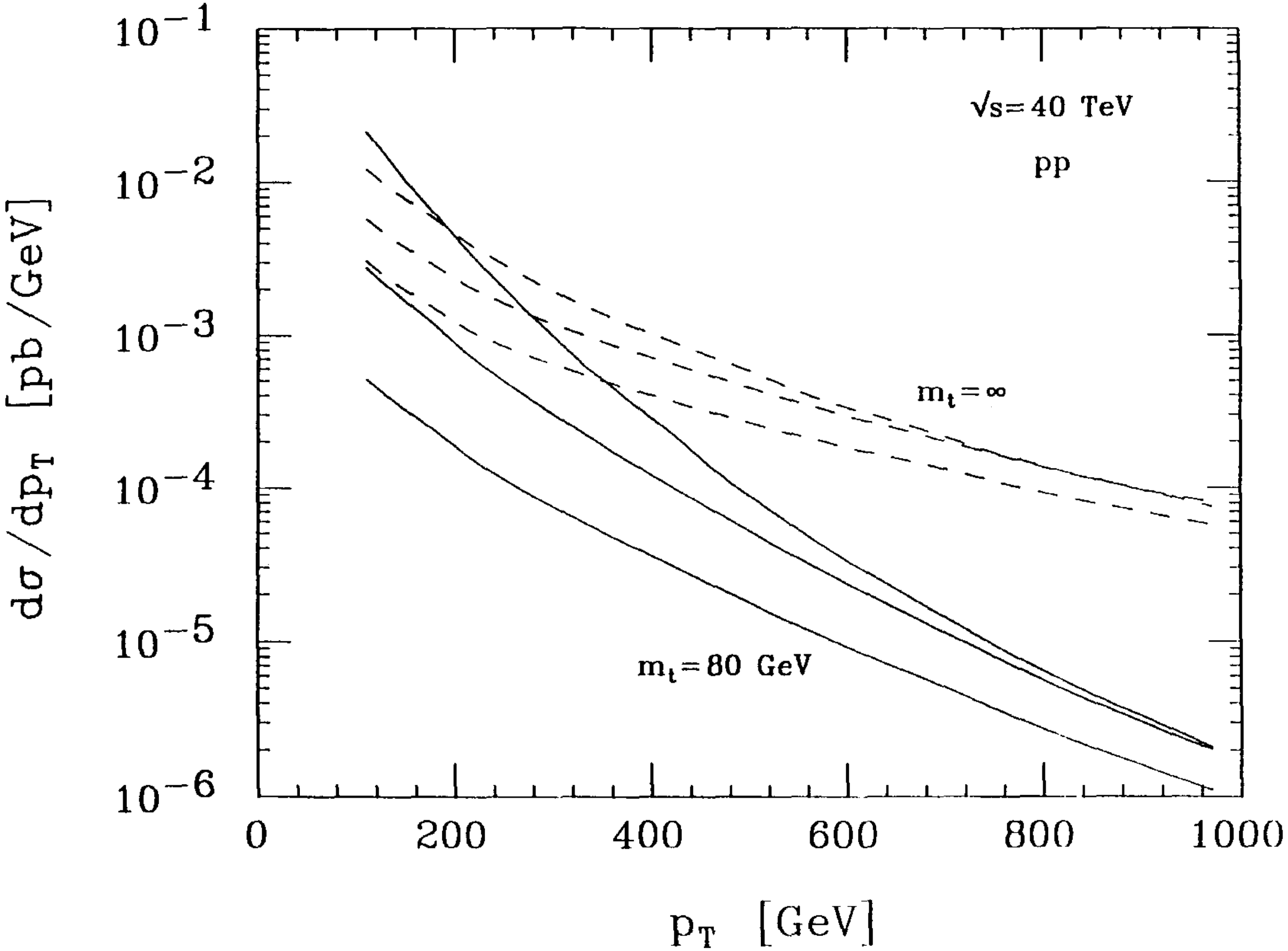
10^{-1}
10^{-2}
10^{-3}
10^{-4}
10^{-5}
10^{-6}
$d\sigma/dp_T$ [pb/GeV]
0
200
400
600
800
1000
p_T [GeV]
$\sqrt{s}=40$ TeV
pp
$m_t=\infty$
$m_t=80$ GeV

Fig. 6

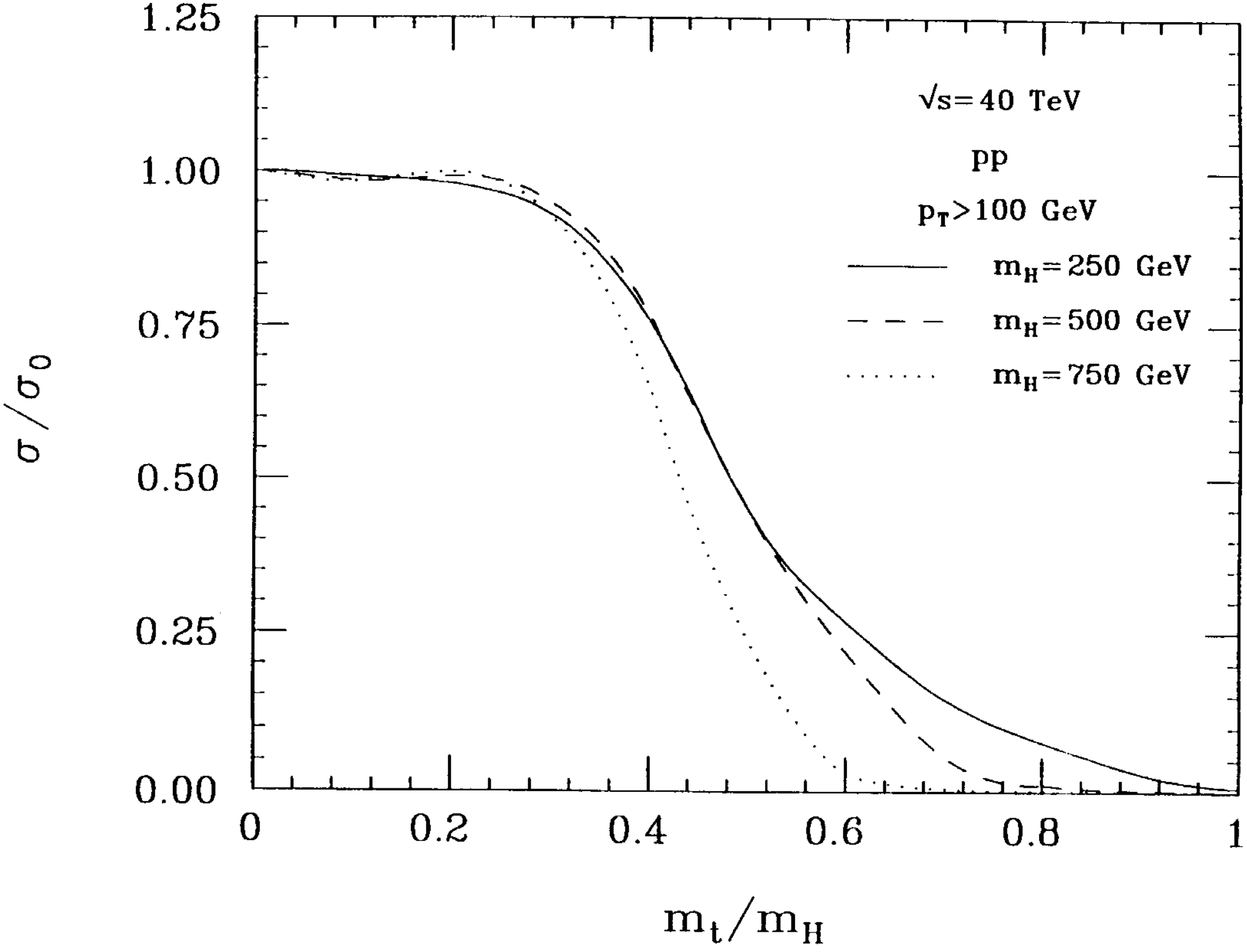
1.25
1.00
0.75
0.50
0.25
0.00
σ/σ_0
0
0.2
0.4
0.6
0.8
1
m_t/m_H
$\sqrt{s}=40$ TeV
pp
$p_T>100$ GeV
$m_H=250$ GeV
$m_H=500$ GeV
$m_H=750$ GeV

Fig. 7

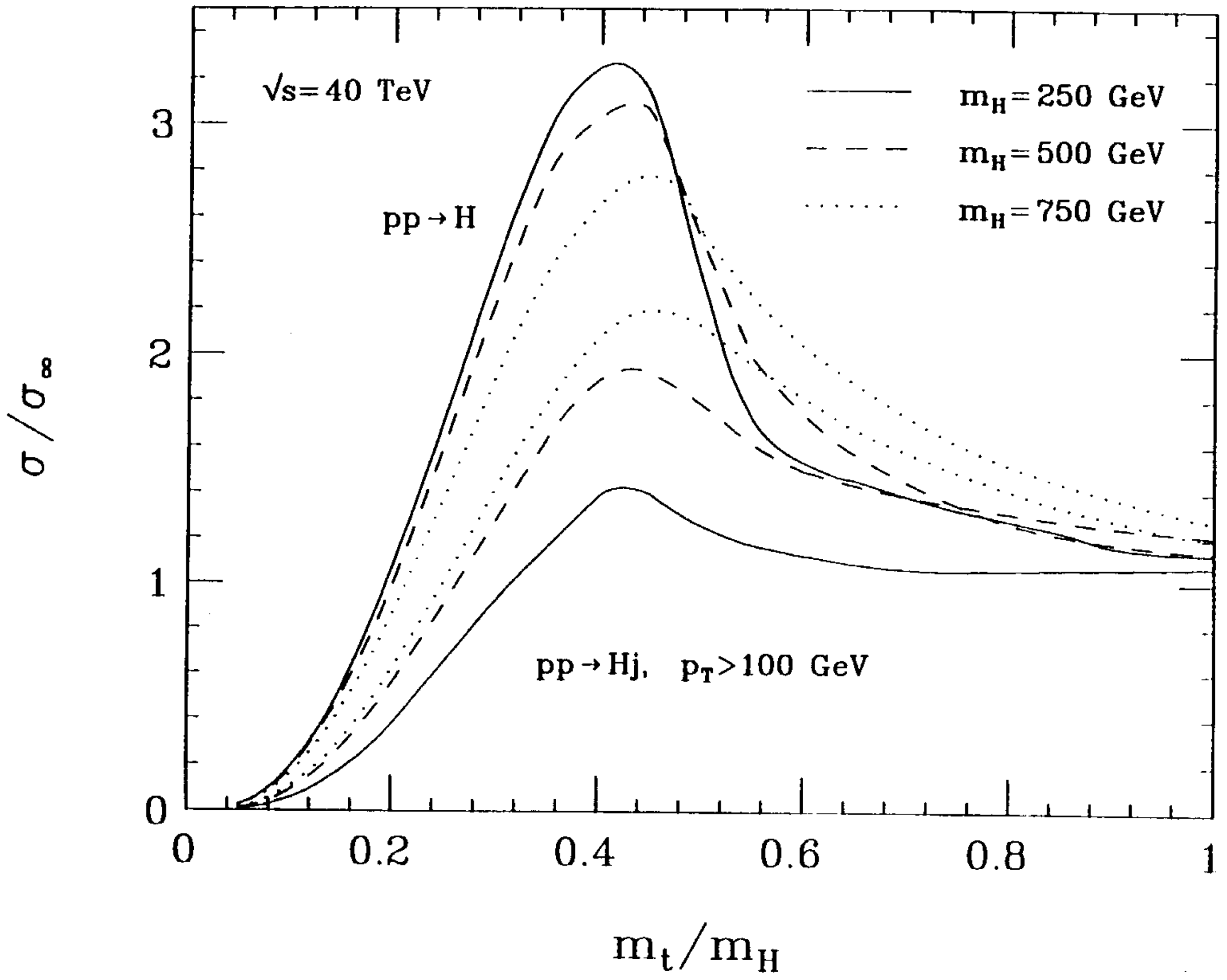
√s=40 TeV
pp → H
pp → Hj, p_T>100 GeV
m_H=250 GeV
m_H=500 GeV
m_H=750 GeV
σ/σ_∞
m_t/m_H
0
1
2
3
0
0.2
0.4
0.6
0.8
1

Fig. 8a

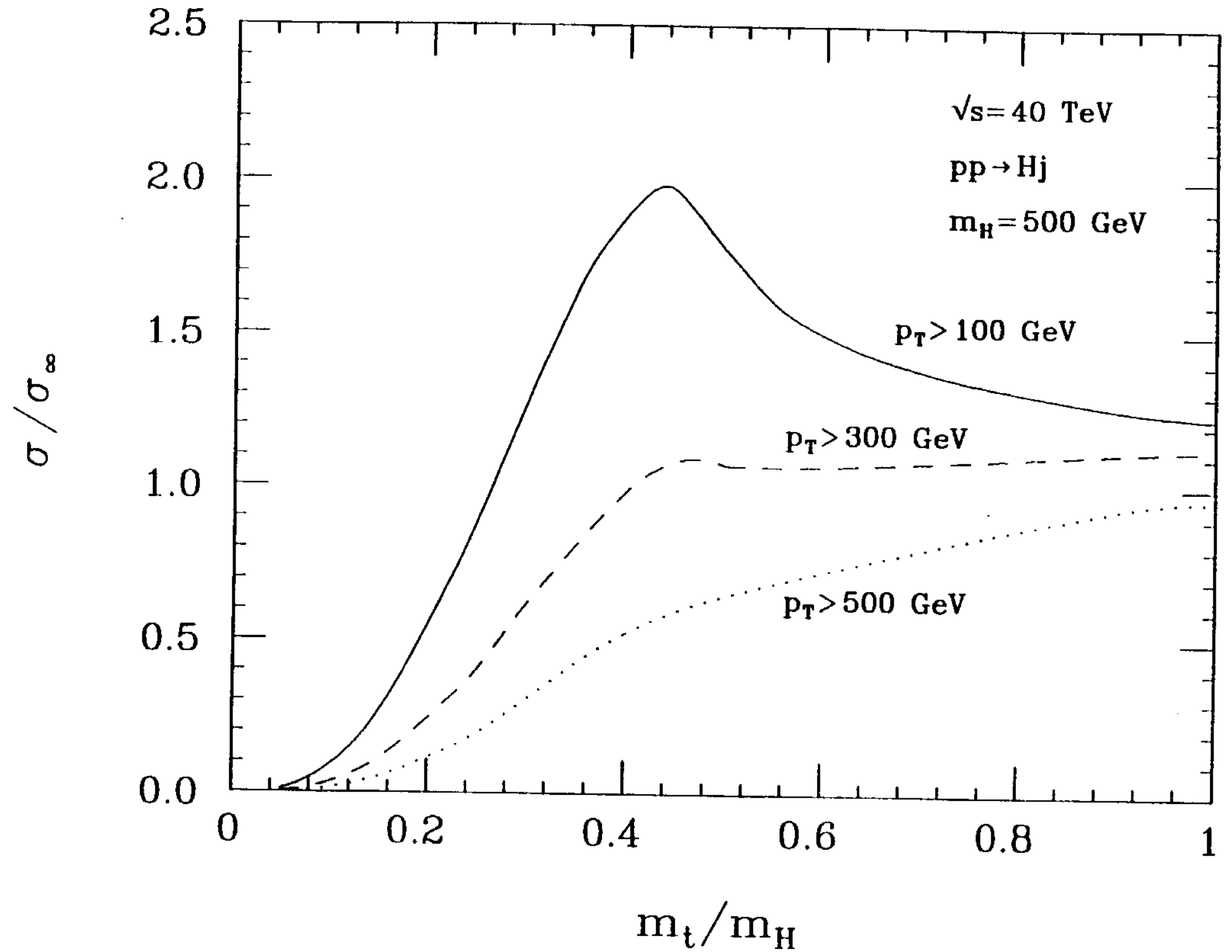

2.5
2.0
1.5
1.0
0.5
0.0
σ/σ_∞
0
0.2
0.4
0.6
0.8
1
m_t/m_H
$\sqrt{s}=40$ TeV
$pp \to Hj$
$m_H=500$ GeV
$p_T>100$ GeV
$p_T>300$ GeV
$p_T>500$ GeV

Fig. 8b

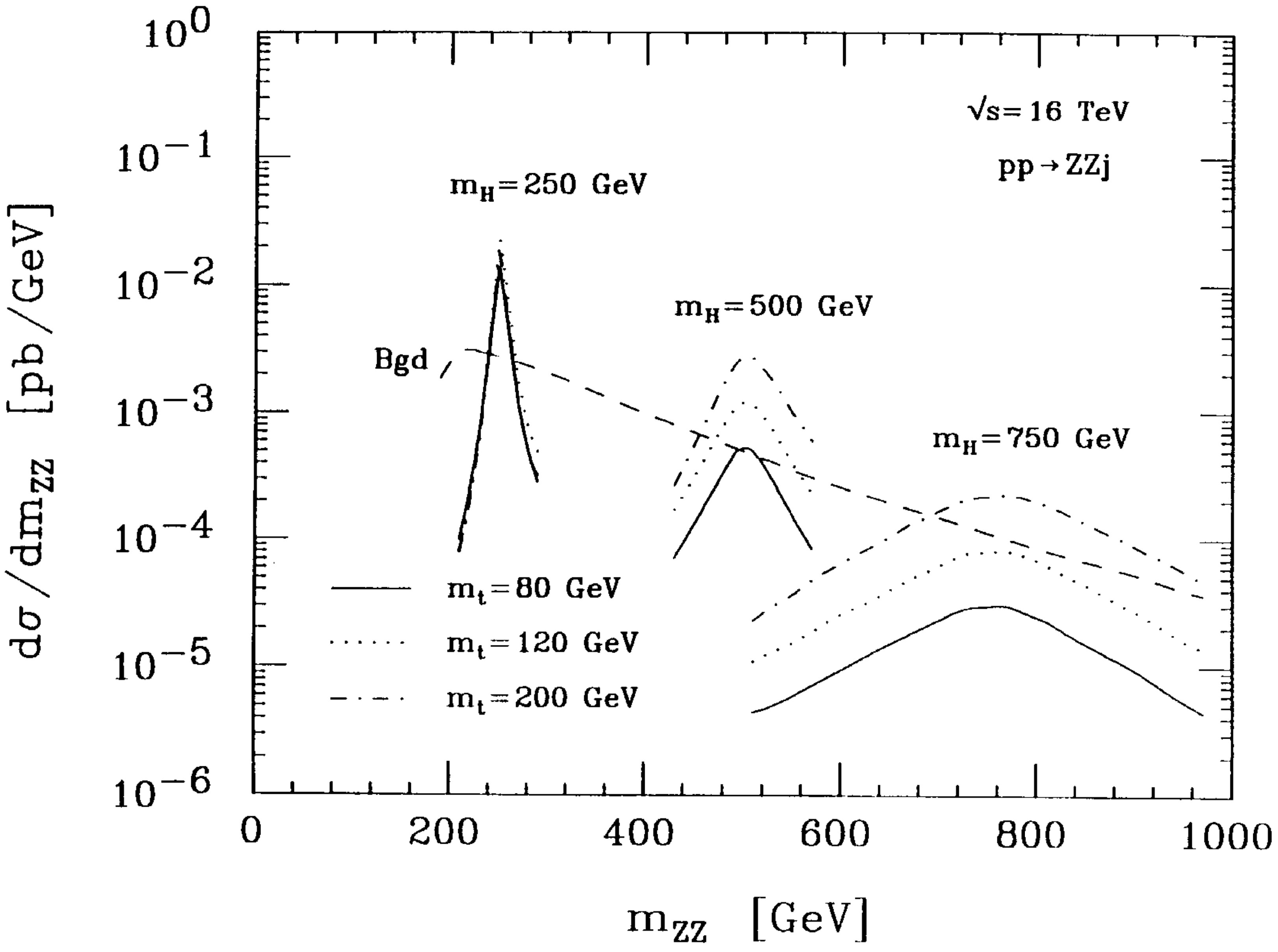
10^0
10^{-1}
10^{-2}
10^{-3}
10^{-4}
10^{-5}
10^{-6}
$d\sigma/dm_{ZZ}$ [pb/GeV]
0
200
400
600
800
1000
m_{ZZ} [GeV]
$\sqrt{s} = 16$ TeV
$pp \to ZZj$
$m_H = 250$ GeV
$m_H = 500$ GeV
$m_H = 750$ GeV
Bgd
$m_t = 80$ GeV
$m_t = 120$ GeV
$m_t = 200$ GeV

Fig. 9a

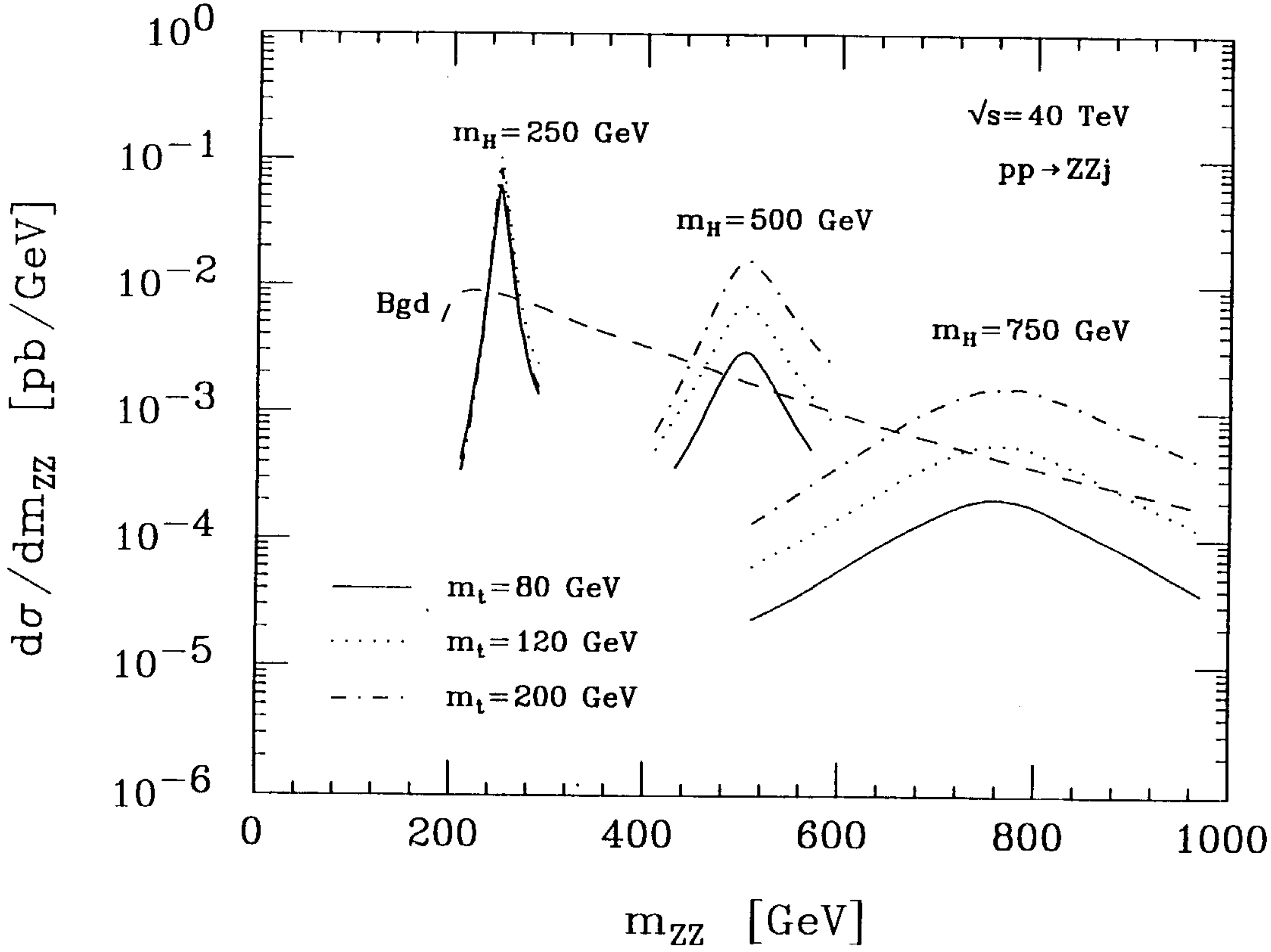
$d\sigma/dm_{ZZ}$ [pb/GeV]
10^0
10^{-1}
10^{-2}
10^{-3}
10^{-4}
10^{-5}
10^{-6}
0
200
400
600
800
1000
m_{ZZ} [GeV]
$\sqrt{s}$=40 TeV
pp → ZZj
m_H=250 GeV
m_H=500 GeV
m_H=750 GeV
Bgd
m_t=80 GeV
m_t=120 GeV
m_t=200 GeV

Fig. 9b

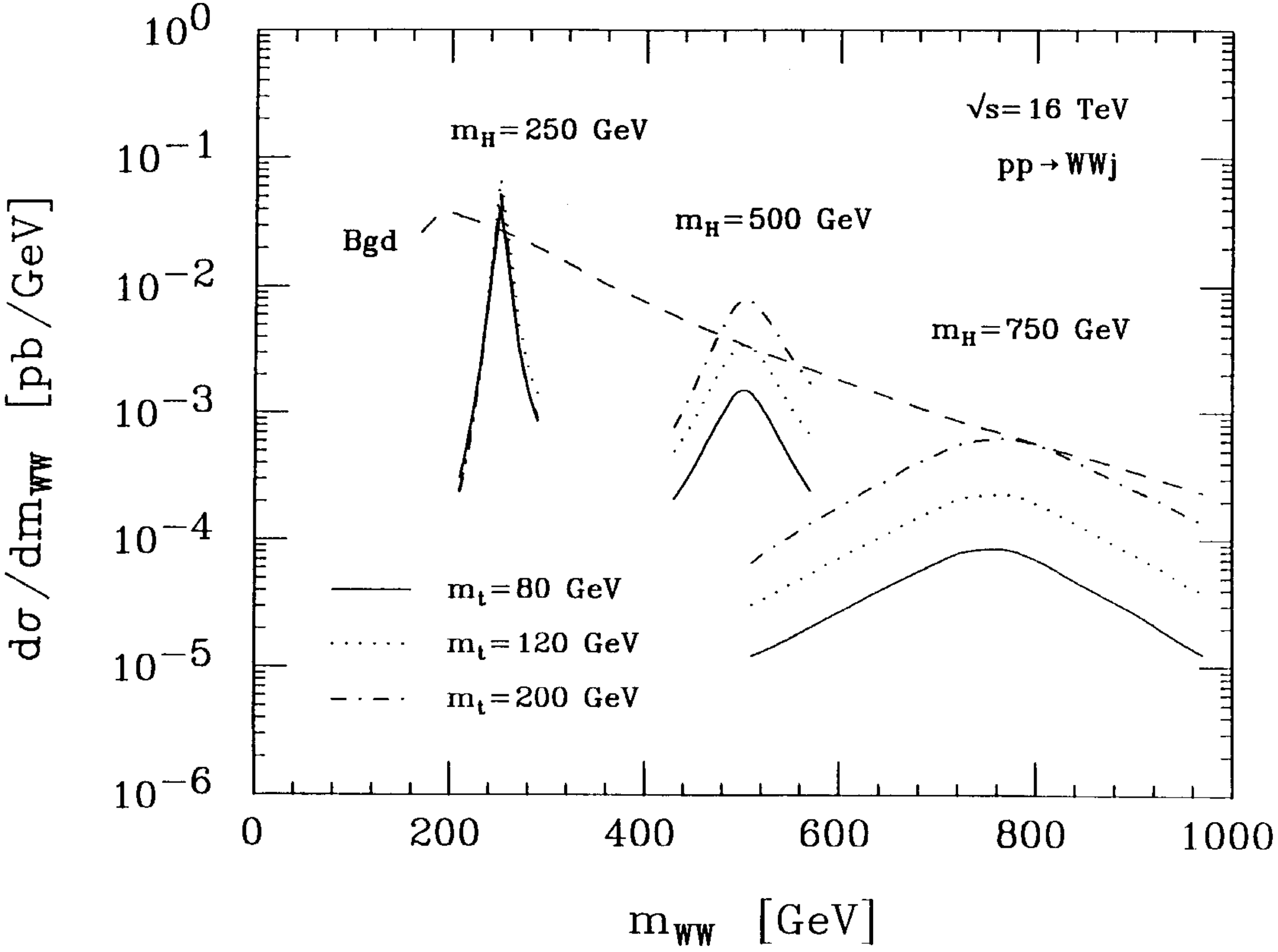
10^0
10^{-1}
10^{-2}
10^{-3}
10^{-4}
10^{-5}
10^{-6}
$d\sigma/dm_{WW}$ [pb/GeV]
0
200
400
600
800
1000
m_{WW} [GeV]
$\sqrt{s}=16$ TeV
$pp \to WWj$
$m_H=250$ GeV
$m_H=500$ GeV
$m_H=750$ GeV
Bgd
$m_t=80$ GeV
$m_t=120$ GeV
$m_t=200$ GeV

Fig. 10a

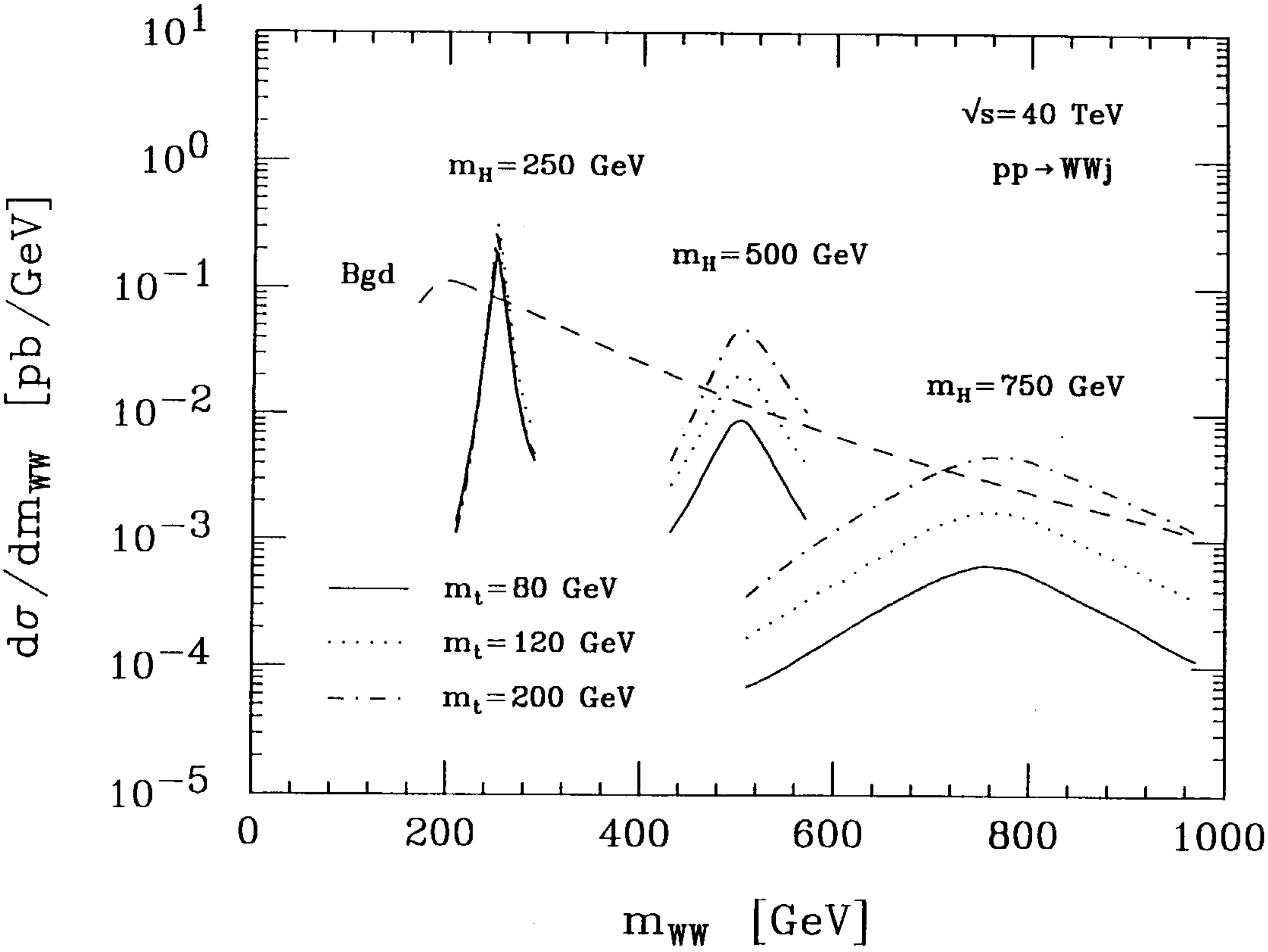

$\sqrt{s}=40$ TeV
$pp \to WWj$
$m_H=250$ GeV
$m_H=500$ GeV
$m_H=750$ GeV
Bgd
$m_t=80$ GeV
$m_t=120$ GeV
$m_t=200$ GeV
10^1
10^0
10^{-1}
10^{-2}
10^{-3}
10^{-4}
10^{-5}
0
200
400
600
800
1000
$d\sigma/dm_{WW}$ [pb/GeV]
m_{WW} [GeV]

Fig. 10b

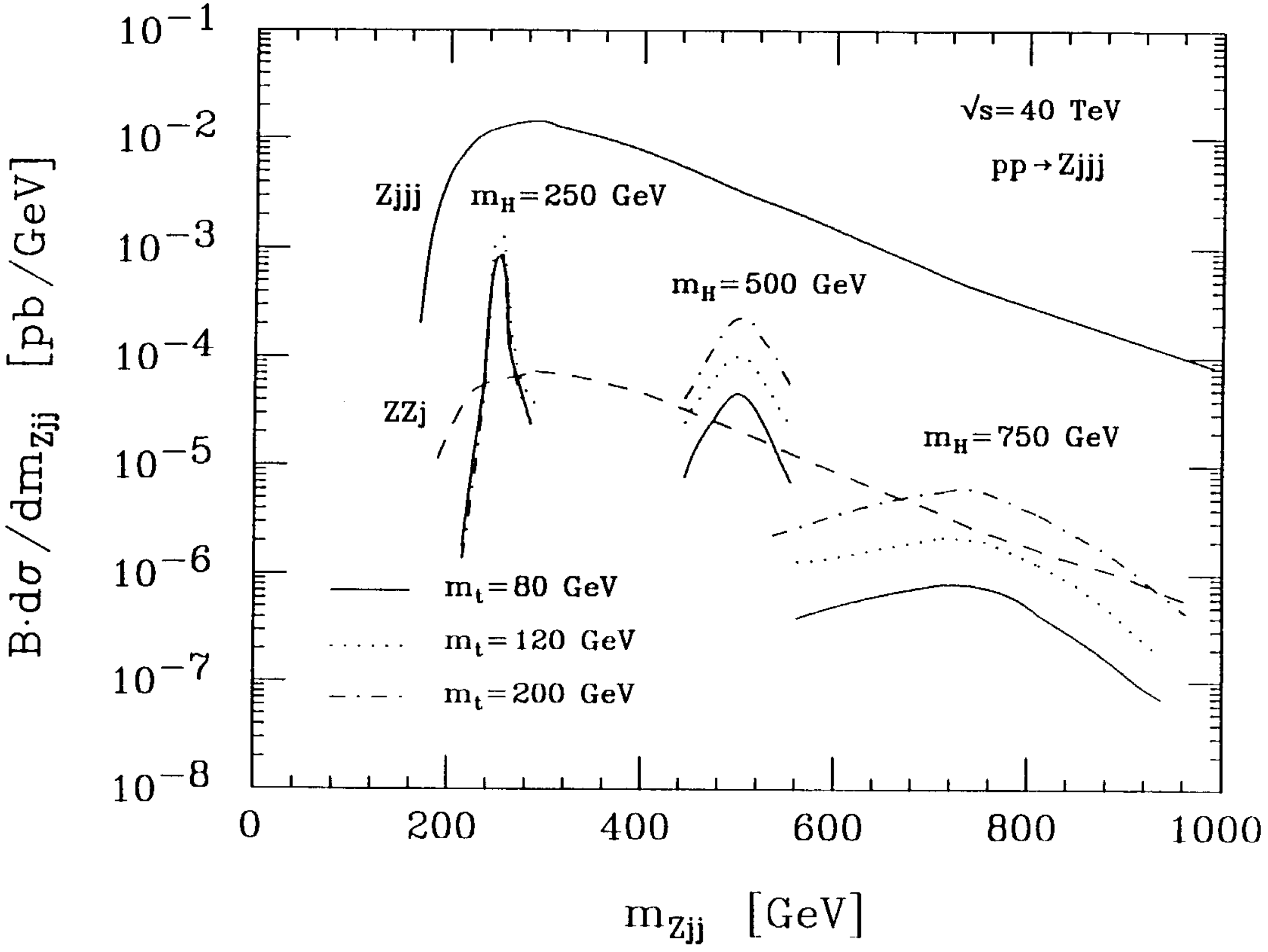
10^{-1}
10^{-2}
10^{-3}
10^{-4}
10^{-5}
10^{-6}
10^{-7}
10^{-8}
$B \cdot d\sigma / dm_{Zjj}$ [pb/GeV]
0
200
400
600
800
1000
m_{Zjj} [GeV]
$\sqrt{s} = 40$ TeV
$pp \to Zjjj$
Zjjj
$m_H = 250$ GeV
$m_H = 500$ GeV
$m_H = 750$ GeV
ZZj
$m_t = 80$ GeV
$m_t = 120$ GeV
$m_t = 200$ GeV

Fig. 11

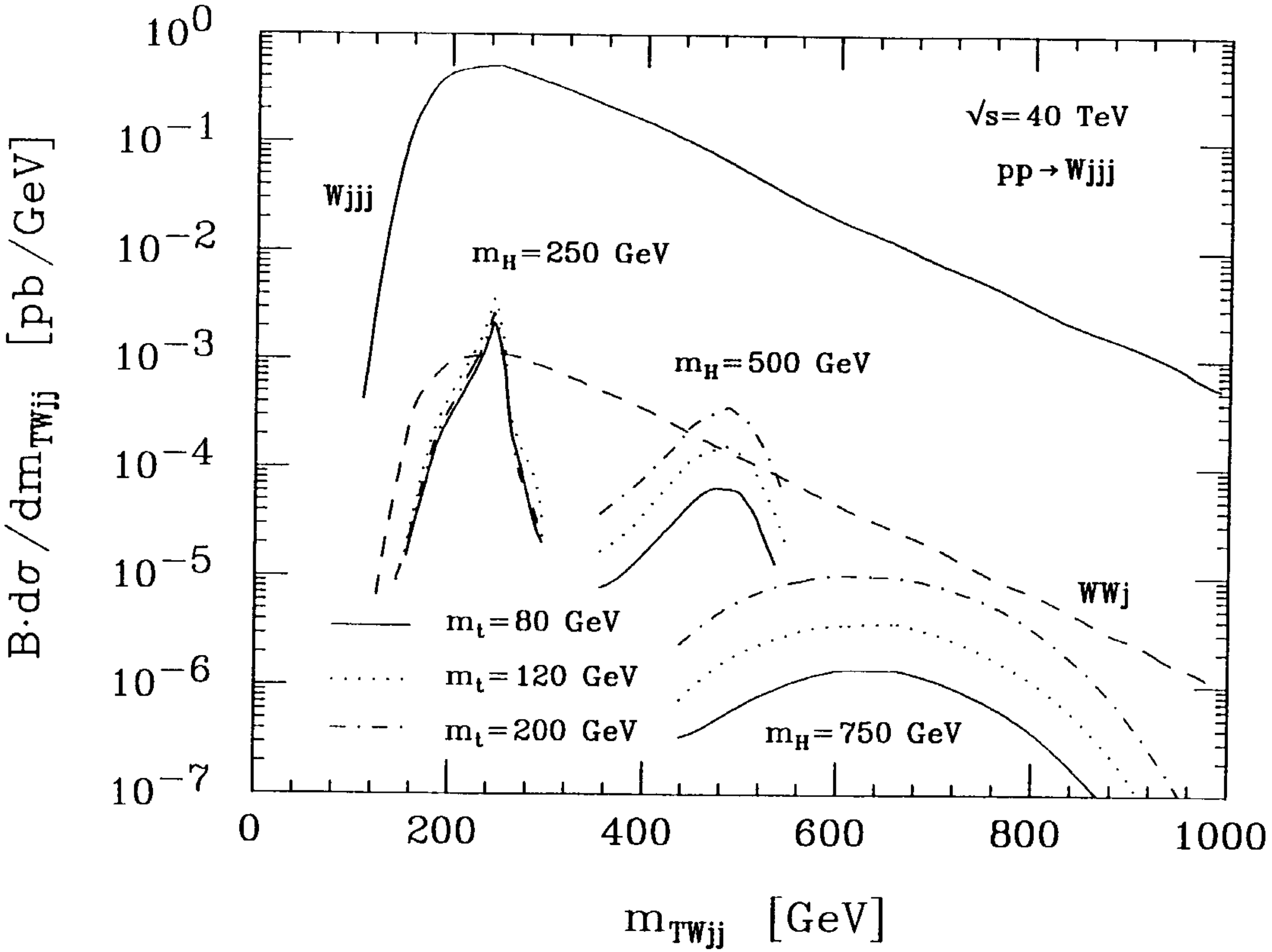

10^0
10^{-1}
10^{-2}
10^{-3}
10^{-4}
10^{-5}
10^{-6}
10^{-7}
$B \cdot d\sigma / dm_{TWjj}$ [pb/GeV]
0
200
400
600
800
1000
m_{TWjj} [GeV]
Wjjj
$\sqrt{s} = 40$ TeV
$pp \to Wjjj$
$m_H = 250$ GeV
$m_H = 500$ GeV
$m_H = 750$ GeV
WWj
$m_t = 80$ GeV
$m_t = 120$ GeV
$m_t = 200$ GeV

Fig. 12